NTNU

Norwegian University of
Science and Technology

Stability and Non-Linear Behaviour of Phase-Locked Loops used in Single-Phase Voltage Source Converters

Sigurd Jarand Strømsem

Master of Science in Cybernetics and Robotics
Submission date: April 2018
Supervisor: Marta Maria Cabrera Molinas, ITK
Co-supervisor: Noe Barrera Gallegos, ITK

Norwegian University of Science and Technology
Department of Engineering Cybernetics

Abstract

A robust phase synchronization system is essential for operating a voltage source converter connected to the electrical grid. The most widespread synchronization technique for single-phase systems is the synchronous reference frame (SRF)-phase-locked loop (PLL). Stability of the SRF-PLL applied to power converter systems has been the subject of numerous studies, though its behaviour has always been assumed linear.

In this thesis relevant literature on the non-linear properties of the phase-locked loop is reviewed and applied to the SRF-PLL. The SRF-PLL is shown to be globally stable using a previously derived Lyapunov function. In addition, a non-linear effect called cycle slips, where the phase-locked loop is leaping between multiple 2π-periodic equilibria, is identified in the literature. The results, obtained by numerical simulation, demonstrate how cycle slips can occur when the voltage source converter is connected to a weak grid, and lead to instability in the power output of the converter.

Connecting non-linear theory developed for general phase-locked loop applications to phenomena observed in power converter systems has not been done before. This thesis does not deliver any control solutions to the problems presented, but should be an important step toward fully understanding the phase-locked loop used in power converters and its limitations.

Sammendrag

En essensiel del av en spenningskilde-omformer koblet til et strømnett er et robust fasesynkroniseringssystem. Den mest utbredte synkroniseringsteknikken som brukes i enfasesystemer kalles synkron referanseramme faselåst sløyfe (SRF-PLL). Stabiliteten til en SRF-PLL brukt i kraftomformere har vært gjenstand for en rekke studier, men oppførselen til systemet har alltid blitt antatt å være lineær.

I denne oppgaven har relevant litteratur knyttet til ikke-linær oppførsel og egenskaper i faselåste sløyfer blitt anvendt på SRF-PLLen brukt i kraftomformere. Synkroniseringssløyfen har blitt bevist å være globalt stabil med en Lyapunov-funksjon fra den teoretiske litteraturen. I tillegg har en ikke-lineær, uønsket effekt blitt identifisert der sløyfen hopper over 2π-periodiske sykluser. Resultatene i oppgaven er funnet med numerisk simulering og viser at syklus-hopp kan oppstå når omformeren er tilkoblet et svakt strømnett, noe som igjen kan føre til ustabil oppførsel og oscillasjon i omformerens effekt-output.

Å knytte ikke-lineær teori utviklet for generelle faselåst sløyfe-applikasjoner til fenomener observert i kraftomformere har aldri blitt gjort før. Selv om denne oppgaven ikke inneholder noen løsning på de beskrevne problemene, tror forfatteren fortsatt at den vil være et viktig steg mot en fullstendig forståelse av faselåste sløyfer i kraftomformere og deres begrensninger.

Acknowledgements

I would like to thank my main supervisor Marta Molinas and co-supervisor Noe Barrera Gallegos for helping me find the right direction and taking me seriously from the very beginning. In addition, I have to thank my parents for helping me with proofreading and suggestions for the text. My girlfriend Henriette needs a special thanks for helping me through the difficult period walking the forest of unknown Lyapunov functions, and with typographical stuff for the thesis such as fonts, colours and general aesthetics. Thanks to my flatmates who helped me become a better swimmer.

Contents

Abstract i

Sammendrag iii

Acknowledgements v

Table of Contents viii

List of Figures x

List of Abbreviations xi

List of Symbols xiii

1 Introduction 1
- 1.1 Motivation . . . 1
- 1.2 Thesis Outline . . . 2
- 1.3 Literature Review . . . 2

2 Background Theory 3
- 2.1 VSC Overview . . . 3
- 2.2 Internal Workings of Converter . . . 4
  - 2.2.1 Converter Topologies . . . 4
  - 2.2.2 PWM Signal Generation . . . 5
  - 2.2.3 Average Model . . . 6
- 2.3 DQ0-Transform . . . 7
  - 2.3.1 Three-Phase Clarke Transform . . . 7
  - 2.3.2 Park Transform . . . 8
  - 2.3.3 Single-Phase Clarke Transform . . . 9
- 2.4 Phase-Locked Loop . . . 10
- 2.5 Power Control in the DQ-Frame . . . 11
  - 2.5.1 Inner Current Control Gains . . . 11
  - 2.5.2 Outer Power Control Gains . . . 12
- 2.6 Non-Linear Stability for Autonomous Systems . . . 13

3 Phase-Locked Loops 15
- 3.1 General Terminology . . . 15
- 3.2 Linear Analysis of the SRF-PLL . . . 18

3.2.1 Stability Analysis . . . 18
3.2.2 Controller Gains . . . 19
3.3 Non-Linear Analysis of the SRF-PLL . . . 20
3.3.1 Equilibrium Points Classification . . . 20
3.3.2 Global Stability Analysis . . . 21
3.4 Lock-In Range for SRF-PLL . . . 23
3.5 Special Considerations for Orthogonal Signal Creation . . . 25
3.5.1 Expanded PLL State Model . . . 26
3.5.2 Local Stability Analysis . . . 27
3.5.3 Global Stability Analysis . . . 28
3.5.3.1 Simulations Indicating Global Stabilty . . . 29

4 Results **31**
4.1 VSC Model Verification . . . 32
4.1.1 VSC Connected to Grid . . . 33
4.2 Non-Linear Behaviour in the PLL . . . 35
4.2.1 Intentionally Provoked Cycle Slips . . . 35
4.2.2 Phase Shift in Grid Source . . . 38
4.2.3 Large Power Step . . . 40

5 Discussion **43**
5.1 Phase Shift and Cycle Slips . . . 43
5.2 Power Step and Cycle Slips . . . 44
5.3 Lock-In Range . . . 44
5.4 PLL Parameters . . . 44

6 Conclusion **47**
6.1 Further Work . . . 47

A Equilibrium Point **49**

B Additional Simulations **51**
B.1 Provoked Cycle Slips with Grid Connection . . . 51

C Simulink Models **53**

Bibliography **57**

List of Figures

2.1 Single-phase voltage source converter 3
2.2 Two and three-level converter topology for single-phase systems 4
2.3 Three-level converter output and corresponding filtered voltage signal . . 5
2.4 PWM signals for the switches S_1 and S_2 in the two-level converter 6
2.5 VSC average model 7
2.6 Fixed α-β frame and rotating dq reference frame 9
2.7 Control structure for the SRF-PLL 10
2.8 Block diagram of the power control structure 11

3.1 Acquisition process with input frequency $f = 60\text{Hz}$, initial frequency $f_0 = 15\text{Hz}$ and loop parameters $\omega_n = 0.43\pi f,\ \zeta = 1$. 15
3.2 General PLL structure 16
3.3 Cycle slip for a system with sinusoidal PD and PI-control 17
3.4 Step response showing phase and frequency error with initial conditions $(\theta_0, \omega_0) = 0$ and $\omega_n = 10\omega,\ \omega = 2\pi 60,\ \zeta = 1/\sqrt{2}$. 20
3.5 Various trajectories of the system (3.8) with the red dots as initial conditions. $K_p = 10,\ T_i = 0.02,\ V_s = 1$, which leads to a very under-damped system. 23
3.6 Comparison between analytical expression for $x_{1_{eq}}$ and numerical solution with $\omega_0 = 2\pi 60$ and $\omega = 2\pi 65$. $\zeta = 1$ and $\omega_n = 2\omega$ as PLL parameters. . 28
3.7 Phase plot with $\omega_0 = 2\pi 60$, $\omega = 2\pi 65$, $\zeta = 1$ and $\omega_n = 2\omega$. The plot to the right is a close-up of the orbit in the leftmost plot. 29
3.8 Cycle slip induced in the system (3.48). $\omega_0 = 2\pi 60$, $\omega = 2\pi 65$, $\zeta = 1$ $\omega_n = 2\omega$. 30

4.1 Comparison between average and switching device model with steps in active power reference 32
4.2 Comparison of PLL transient behaviour during acquisition process 33
4.3 Comparison of PLL output at power step change 33
4.4 Comparison between models with grid connection 34
4.5 Comparison of PLL transient behaviour during acquisition process with grid connection 34
4.6 Comparison of PLL output at power step change with grid connection . . 35
4.7 Comparison of active power output for the two models exposed to cycle slips 36
4.8 Comparison of estimated phase angle for the two models exposed to cycle slips 36
4.9 Comparison of estimated frequency for the two models exposed to cycle slips 37

4.10 Phase plot exhibiting the leap from one equilibrium to another 37
4.11 Effect of phase shift in grid source on active power output with weak grid connection 38
4.12 Effect of phase shift on PLL output with weak grid connection 39
4.13 Effect of phase shift on PLL output with weak grid connection 39
4.14 Effect of large power reference step at $t = 0$ on active power output with weak grid connection 40
4.15 Effect of large power reference step at $t = 0$ on $\hat{\theta}$ with weak grid connection 41
4.16 Effect of large power reference step at $t = 0$ on $\hat{\omega}$ with weak grid connection 41
4.17 Phase-plot of phase and frequency error after a large step in power reference was applied 42

B.1 Comparison of active power output for the two models exposed to cycle slips. Note that the last average model simulations was stopped early . . . 51
B.2 Phase plots for the two models exposed to cycle slips. Note that the last average model simulations was stopped early 51

C.1 Simulink model without grid transmission line 53
C.2 Simulink model with grid transmission line 54

Abbreviations

AC	Alternating Current
DC	Direct Current
DQ	Direct-Quadrature
DQ0	Direct-Quadrature-Zero
HVDC	High Voltage Direct Current
LCC	Line Commutated Converter
ODE	Ordinary Differential Equation
PCC	Point of Common Coupling
PD	Phase Detector
PI	Proportional and Integral
PLL	Phase-Locked Loop
PWM	Pulse-Width Modulation
SOGI	Second Order Generalized Integrator
SRF	Synchronous Reference Frame
SRF-PLL	Synchronous Reference Frame Phase-Locked Loop
VCO	Voltage Controlled Oscillator
VSC	Voltage Source Converter

Symbols

Symbol	Description	Unit
I_s	AC current measured at PCC	A
I_{ac}	Actual AC current at VSC terminal	V
I_{dq}	Vector representing AC current in DQ-frame	A
K_p	Proportional gain	-
L_g	AC grid transmission line inductance	H
L_s	VSC filter inductance	H
P	Active power	W
Q	Reactive power	W
R_g	AC grid transmission line resistance	Ω
R_s	VSC filter resistance	Ω
T_i	Integral time constant	-
V_g	AC grid source peak voltage	V
V_m^*	Desired AC voltage measured at VSC terminal	V
V_{ac}	Actual AC voltage at VSC terminal	V
V_{dc}	DC grid source voltage	V
V_{dq}	Vector representing AC voltage in DQ-frame	V
V_s	AC voltage measured at PCC	V
$\hat{\omega}$	Estimated frequency of AC voltage measured at PCC	$\mathrm{rad\,s^{-1}}$
$\hat{\theta}$	Estimated phase angle of AC voltage measured at PCC	rad
ω_0	Initial condition for frequency estimate	$\mathrm{rad\,s^{-1}}$
ω_n	Natural frequency	$\mathrm{rad\,s^{-1}}$
ω	True frequency of AC voltage measured at PCC	$\mathrm{rad\,s^{-1}}$
θ	True phase angle of AC voltage measured at PCC	rad
ζ	Damping coefficient	-
m	Modulation signal for switching devices	-

1 Introduction

1.1 Motivation

During the last century most of the world's power generation and transmission systems used alternating current (AC). This is still the case today, but direct current (DC) generation and transmission is currently on the rise. Photovoltaic cells which produce DC current has seen an exponential drop in price [1] and reached unprecedented levels of efficiency [2]. The costs of sea-based wind generation with DC transmission to land is reaching grid parity as well [3]. In addition, due to its inherent simplicity, low investment cost and low power losses, DC transmission is growing more popular in certain point-to-point applications such as high voltage direct current (HVDC) interconnectors [4].

A prerequisite for all the above applications is very efficient and reliable converters between the AC grid connection and the DC transmission/generation connection. For low power applications such as residential solar generation and other types of microgrids, voltage source converters (VSCs) are used for the connection to the utility grid. In high voltage applications, line commutated converters (LCCs) have been dominant, but during the last 20 years, with the development of fully controllable high-power semiconductor devices, VSCs have become competitive for this type of applications as well. It is expected that all LCCs will be replaced by VSCs in the future [5].

A key component of the VSC is the phase-locked loop (PLL). The PLL is a control system which tracks the frequency and phase angle of the connected utility grid signal. The phase and frequency is then used to form the modulation signal for the semiconductor devices. A good PLL is characterized by fast synchronization, robustness, accuracy and above all, lock in at the correct frequency and phase angle. With a wrong phase and/or frequency prediction, the power output of the VSC is unstable [6]. Surprisingly, little interest has been shown among researchers to investigate possible failure of the PLL. Instead, considerable effort is directed toward improving the performance of the PLL system. In addition, when a stability analysis is presented it has usually been carried out in the linear domain.

The purpose of this thesis is to bring mathematical rigour to the most common single-phase PLL system and investigate possible non-linear behaviour and bounds of stability with non-linear analysis tools. The results from this analysis will hopefully give a definite answer to whether non-linear effects in the PLL that are ignored in linear analysis can lead to instability in the entire VSC.

1.2 Thesis Outline

- Chapter 2 presents background theory for the thesis, specifically the structure and theory behind the VSC. In addition, a brief section on non-linear stability analysis is included for completion.
- In chapter 3 the PLL is analysed in detail. Linear and non-linear analysis results from various references is reviewed and explained. The chapter ends with a section featuring a new state model for the PLL where the orthogonal signals used for the single-phase DQ transform are not ideal.
- Chapter 4 contains the main results for the thesis obtained by numerical simulation. First, a verification of the system is presented, then behaviour under various fault conditions are shown.
- In chapter 5 hypotheses and possible explanations for the results are given, and chapter 6 presents the thesis conclusion and recommended further work.

1.3 Literature Review

Numerous articles and books have been devoted to the study of the phase locked loop for general applications, both in the linear and non-linear domain. In *Almost global stability of phase-locked loops* [7], the author proves global stability for the equivalent of a proportional and integral (PI)-controlled PLL with a sinusoidal non-linearity. The proposed lyapunov function applies only to this very specific case, but the article serves as a good entry point for non-linear PLL analysis. Leonov G.A. et al.[8] derive rigorous formulations of the various ranges which define different behaviour in the PLL. In a later article, *Pull-in range of the PLL-based circuits with proportionally-integrating filter* [9], a Lyapunov function allowing arbitrary non-linearities in the phase detector (PD) (defined in section 3.1) is introduced. The PHD-thesis *Computation of the lock-in ranges of phase-locked loops with PI filter* [10] shows how the lock-in range can be analytically computed for two common non-linear phase detectors. The lock-in range describes the boundary between where cycle slips will and will not occur. Cycle slips are an unwanted non-linear effect of the PLLs differential equations which leads to large errors in the phase and frequency estimates.

J. Z. Zhou et al.[6] show how the VSC can exhibit unstable operation when the reference for the power controller is changed, and the instability is traced to the PLL control parameters. No further explanation for the cause of failure is provided. The method of provoking unstable behaviour by changing the power reference is used in this thesis.

2 | Background Theory

2.1 VSC Overview

A VSC is used to transfer power between AC and DC networks, and acts as the main intersection. Traditionally this task has been reserved for LCCs, which perform adequately, but consume significant amounts of reactive power and suffer from lack of waveform quality [5]. With the development of fully controllable high-power semiconductors, it became possible to build converters with properties previously seen in computer science and low voltage applications only. Such a converter can reproduce any waveform up to a limiting frequency, and can control power flow in both directions [11]. In addition, with specific control strategies, the reactive and active power flow can be controlled independently [12].

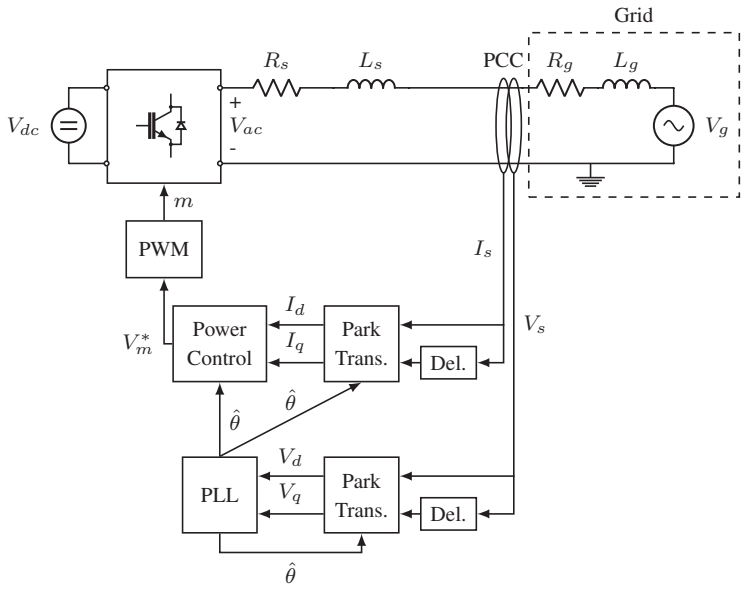

Figure 2.1: Single-phase voltage source converter

An overview of a single-phase converter system is shown in fig. 2.1. It features some key components, namely the actual converter containing the semiconductor devices, the pulse width modulation (PWM) system generating the gate signal from the reference voltage V_m^*, the power controller and the phase-locked loop responsible for tracking the phase and frequency of the utility voltage. In addition a RL-filter is applied at the VSC terminal to

ensure a smooth sine signal is injected into the grid. The intersection between the grid and the converter where the voltage and current measurements V_s and I_s are made, is referred to as the point of common coupling (PCC).

2.2 Internal Workings of Converter

2.2.1 Converter Topologies

The large block in fig. 2.1 contains the circuitry where the actual transfer of power between the AC and DC side occur. Two simple converter topologies are shown in fig. 2.2. The two level converter shown on the left operates by toggling S_1 and S_2 alternately according to the PWM signal. When the PWM signal m is correct and the VSC terminal filter is tuned properly, the measured voltage, V_s, appears as a sinusoidal wave synchronized to the utility voltage at PCC.

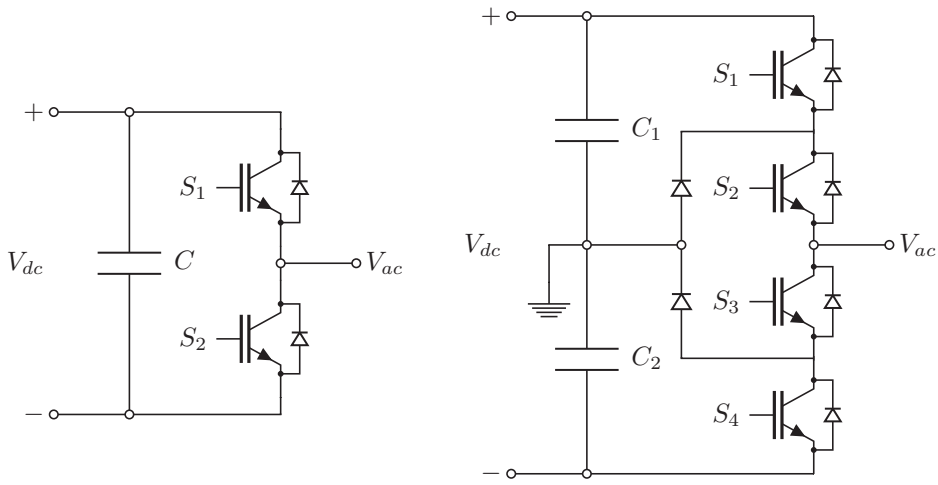

Figure 2.2: Two and three-level converter topology for single-phase systems

Three-level neutral-point-clamped topology is more complex than the two-level structure, but provides higher accuracy. It has three modes of operation, $S_1,\ S_2$ closed and the rest open, $S_2,\ S_3$ closed and the rest open or $S_3,\ S_4$ closed and the rest open. It is easy to see that the output, V_{ac}, is $V_{dc},\ 0$ and $-V_{dc}$ respectively. As with the two-level converter, this signal appears as a smooth sine wave at the output, given a proper PWM signal and terminal filter. Fig. 2.3 displays the converter output of a three-level converter and the corresponding sinusoidal voltage injected into the grid. The AC waveform is slightly phase delayed due to the inductance in the VSC terminal filter.

In addition to the topologies depicted in fig. 2.2 there exists numerous additional structures, however the working principle remains the same.

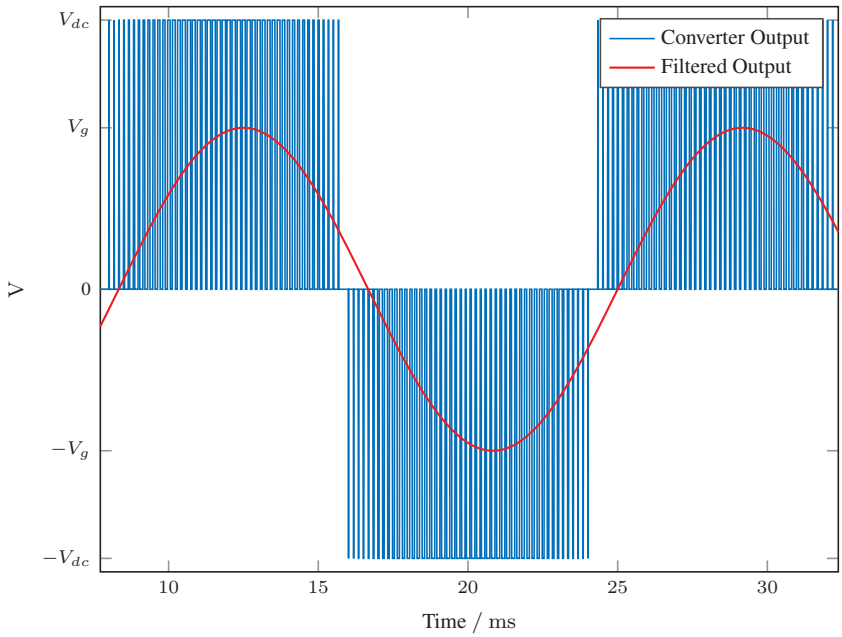

Figure 2.3: Three-level converter output and corresponding filtered voltage signal

2.2.2 PWM Signal Generation

As seen in the previous section, a signal for alternate switching of the semiconductor devices is required to construct the desired signal at the VSC terminal. A common way to generate these signals is by comparing a high-frequency carrier wave with the desired modulation signal. As we see from fig. 2.4, the intersection between the carrier wave and the modulation signal determine when the switches turn on and off. When the carrier wave is larger than V_m^*, S_1 is closed and S_2 is opened (fig. 2.2). When the carrier is smaller than V_m^*, S_1 is opened and S_2 is closed. Some modification is required for other converter structures, but the main principle remains the same.

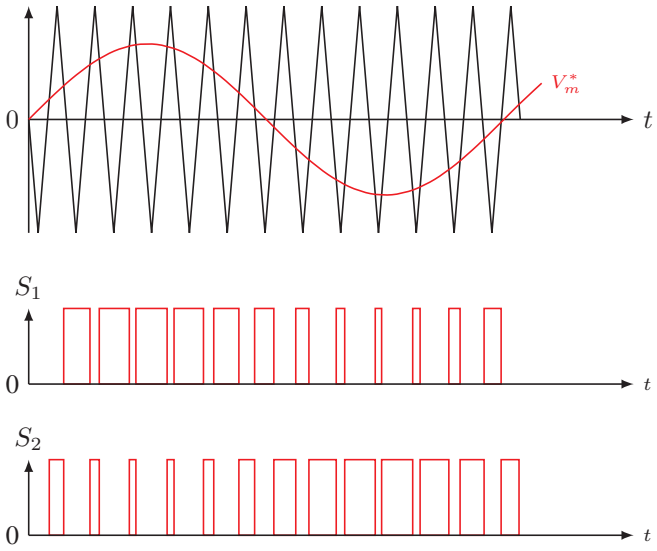

Figure 2.4: PWM signals for the switches S_1 and S_2 in the two-level converter

2.2.3 Average Model

Modelling the internal workings of the converter depend heavily on the chosen converter topology, but in cases where the long term (long term in relation to the converter switching frequency) operation is being studied, a time-averaged converter model will be sufficient. From [13] the relation between the AC and DC side is

$$V_{ac} = mV_{dc}, \tag{2.1}$$

where m is a function representing the average PWM generated signal. The AC side can be modelled by a controlled voltage source consuming the power $V_{ac}I_{ac}$ and the DC side as a controlled current source being injected with the power $V_{dc}I_{dc}$ (see fig. 2.5). Assuming conservation of power we obtain the following relations between the two sides (2.2). In a real scenario, conservation of power is probably not exactly true, due to some internal resistance in the semiconductor devices.

$$\begin{aligned} P_{ac} = P_{dc} \implies V_{ac}I_{ac} = V_{dc}I_{dc} \\ \implies I_{dc} = mI_{ac} \end{aligned} \tag{2.2}$$

If we apply Kirchoff's voltage law between the converter and the voltage at PCC, V_s, we find the differential equation for the AC current flowing in to the AC grid (2.3).

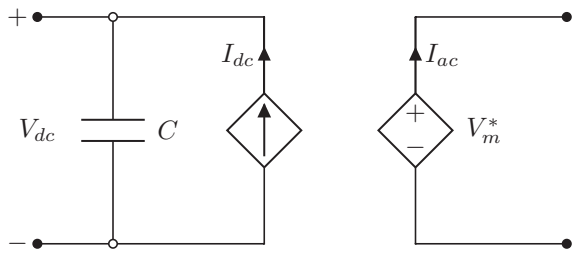

Figure 2.5: VSC average model

$$\frac{dI_{ac}}{dt} = \frac{1}{L_s}(V_{ac} - I_{ac}R_s - V_s) = \frac{1}{L_s}(mV_{dc} - I_{ac}R_s - V_s) \tag{2.3}$$

2.3 DQ0-Transform

The direct-quadrature-zero (DQ0) transform is used to convert AC signals to equivalent DC signals in another frame of reference. More specifically, the transform consists of a mapping of the three AC waveforms in a three-phase system into a two-phase coordinate system (known as the $\alpha\beta 0$ or the Clarke transform (2.4)). Then the two phases are translated into a rotating reference frame (DQ frame) using the Park transformation. For a three-phase system the DQ0 transform is the product of the Clarke and Park transform. For a single-phase system we need to apply some creativity to artificially construct the two phases, which for a three-phase system is provided by the Clarke transform.

2.3.1 Three-Phase Clarke Transform

The Clarke transform for a three-phase system is shown in (2.4).

$$T = \frac{2}{3}\begin{pmatrix} 1 & -\frac{1}{2} & -\frac{1}{2} \\ 0 & \frac{\sqrt{3}}{2} & -\frac{\sqrt{3}}{2} \\ \frac{1}{2} & \frac{1}{2} & \frac{1}{2} \end{pmatrix} \tag{2.4}$$

$$V_s = \begin{pmatrix} V_s\cos(\omega t) \\ V_s\cos(\omega t - \frac{2\pi}{3}) \\ V_s\cos(\omega t + \frac{2\pi}{3}) \end{pmatrix} \tag{2.5}$$

Assuming a balanced three-phase system as (2.5) we get

$$TV_s = \begin{pmatrix} \frac{2}{3}V_s(\cos(\omega t) - \frac{1}{2}\cos(\omega t - \frac{2\pi}{3}) - \frac{1}{2}\cos(\omega t + \frac{2\pi}{3})) \\ \frac{\sqrt{3}}{3}V_s(\cos(\omega t - \frac{2\pi}{3}) + \cos(\omega t + \frac{2\pi}{3})) \\ \frac{1}{3}V_s(\cos(\omega t) + \cos(\omega t - \frac{2\pi}{3}) + \cos(\omega t + \frac{2\pi}{3})) \end{pmatrix}. \tag{2.6}$$

From trigonometry we have the following relations

$$\cos(\theta)\cos(\varphi) = \frac{1}{2}\cos(\theta - \varphi) + \frac{1}{2}\cos(\theta + \varphi), \tag{2.7a}$$

$$\sin(\theta)\sin(\varphi) = \frac{1}{2}\cos(\theta - \varphi) - \frac{1}{2}\cos(\theta + \varphi). \tag{2.7b}$$

The Clarke transformation applied to the balanced three-phase system is then found as

$$TV_s = \begin{pmatrix} V_\alpha \\ V_\beta \\ V_0 \end{pmatrix} = \begin{pmatrix} \frac{2}{3}V_s(\cos(\omega t) - \cos(\omega t)\cos(\frac{2\pi}{3})) \\ \frac{1}{3}V_s(2\sin(\omega t)\sin(\frac{2\pi}{3})) \\ \frac{1}{3}V_s(\cos(\omega t) + 2\cos(\omega t)\cos(\frac{2\pi}{3})) \end{pmatrix} = \begin{pmatrix} V_s\cos(\omega t) \\ V_s\sin(\omega t) \\ 0 \end{pmatrix}. \tag{2.8}$$

2.3.2 Park Transform

The second part of the DQ0 transform is the Park transform, which is identical for single-phase and three-phase systems. The two reference frames are shown in fig. 2.6. The DQ frame is defined as a coordinate system rotating with frequency ω. The change of basis from the stationary α-β reference frame to the DQ frame is found by expressing the unit vectors of the DQ coordinate system in the stationary system.

$$e_d = (\cos(\theta(t)), \sin(\theta(t))) \tag{2.9a}$$

$$e_q = (\cos(\theta(t) + \frac{\pi}{2}), \sin(\theta(t) + \frac{\pi}{2})) = (-\sin(\theta(t)), \cos(\theta(t))) \tag{2.9b}$$

We see that $e_{dq} = \begin{pmatrix} e_d & e_q \end{pmatrix}^\top$ is identical to the standard rotation matrix for a two-dimensional Cartesian coordinate system with a negative $\theta(t)$. The relations in (2.10) and (2.11) show the transformation to and from the DQ frame for the arbitrary vector $V_{\alpha\beta}$.

$$V_{dq} = \begin{pmatrix} V_d \\ V_q \end{pmatrix} = R(-\theta)V_{\alpha\beta}, \quad R(-\theta) = R(\theta)^\top = \begin{pmatrix} \cos(\theta) & \sin(\theta) \\ -\sin(\theta) & \cos(\theta) \end{pmatrix} \tag{2.10}$$

$$V_{\alpha\beta} = \begin{pmatrix} V_\alpha \\ V_\beta \end{pmatrix} = R(\theta)V_{dq}, \quad R(\theta) = \begin{pmatrix} \cos(\theta) & -\sin(\theta) \\ \sin(\theta) & \cos(\theta) \end{pmatrix} \tag{2.11}$$

Inserting the results from (2.8) and using the fact that $\theta = \omega t$ we find the following expression for V_{dq}, which applies to a perfectly balanced three-phase system where the angle θ is known.

$$V_{dq} = \begin{pmatrix} V_s(\cos^2(\theta) + \sin^2(\theta)) \\ V_s(-\cos(\theta)\sin(\theta) + \cos(\theta)\sin(\theta)) \end{pmatrix} = \begin{pmatrix} V_s \\ 0 \end{pmatrix} \tag{2.12}$$

The equations for instantaneous active and reactive power in the DQ frame is

$$P = V_d I_d + V_q I_q \tag{2.13a}$$
$$Q = V_q I_d - V_d I_q, \tag{2.13b}$$

where I_d and I_q is found with the DQ0 transform. This reduces to

$$P = V_d I_d \tag{2.14a}$$
$$Q = -V_d I_q \tag{2.14b}$$

when the reference frame is synchronized to the voltage, and show that the active and reactive power can be controlled separately, assuming independent current control of I_d and I_q.

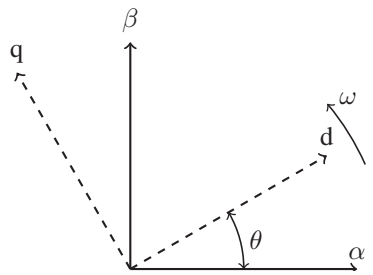

Figure 2.6: Fixed α-β frame and rotating dq reference frame

2.3.3 Single-Phase Clarke Transform

Currently an analogue to the three-phase Clarke transform does not exist for single-phase systems. However, a widely used method is to delay the input signal by $\varphi = \frac{\pi}{2}$. For a frequency ω we obtain the same result as (2.8) in (2.15).

$$V_{\alpha\beta} = \begin{pmatrix} V_s \cos(\omega t) \\ V_s \cos(\omega t - \frac{\pi}{2}) \end{pmatrix} = \begin{pmatrix} V_s \cos(\omega t) \\ V_s \sin(\omega t) \end{pmatrix} \tag{2.15}$$

2.4 Phase-Locked Loop

As seen in section 2.3.2 the DQ0 transform can translate a three-phase or single-phase AC signal to two DC signals when the phase angle θ is known. In a real world scenario this is not the case, and the angle needs to be estimated. This is commonly handled by the PLL. The synchronous reference frame (SRF)-PLL is the most widespread estimation method for obtaining the phase and frequency of the input AC waveforms [14], however multiple variations and improvement exist. The structure for the SRF-PLL is shown in fig. 2.7.

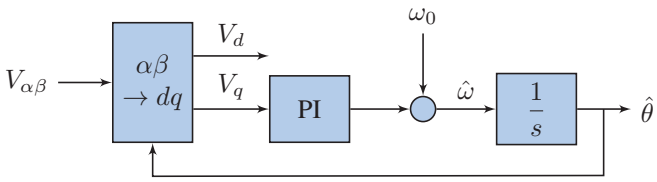

Figure 2.7: Control structure for the SRF-PLL

As the true phase angle θ and frequency ω are unknown, the estimated values $\hat{\theta}$, $\hat{\omega}$ are used in the Park transform to obtain V_{dq}. Eq. (2.10) is then rewritten as

$$V_{dq} = \begin{pmatrix} \cos(\hat{\theta}) & \sin(\hat{\theta}) \\ -\sin(\hat{\theta}) & \cos(\hat{\theta}) \end{pmatrix} V_{\alpha\beta}. \tag{2.16}$$

With $V_{\alpha\beta}$ as defined in both (2.8) and (2.15) we find that

$$\begin{aligned} V_{dq} = \begin{pmatrix} V_d \\ V_q \end{pmatrix} &= \begin{pmatrix} V_s \cos(\omega t)\cos(\hat{\theta}) + V_s \sin(\omega t)\sin(\hat{\theta}) \\ -V_s \cos(\omega t)\sin(\hat{\theta}) + V_s \sin(\omega t)\cos(\hat{\theta}) \end{pmatrix} \\ &= \begin{pmatrix} V_s \cos(\hat{\theta} - \theta) \\ -V_s \sin(\hat{\theta} - \theta) \end{pmatrix}, \end{aligned} \tag{2.17}$$

from which it is easy to see that we obtain the correct phase prediction when regulating V_q to zero. The differential equations for the SRF-PLL is then derived as

$$\begin{pmatrix} \dot{\gamma} \\ \dot{\hat{\theta}} \end{pmatrix} = \begin{pmatrix} -V_s \sin(\hat{\theta} - \theta) \\ K_p(-V_s \sin(\hat{\theta} - \theta) + \frac{1}{T_i}\gamma) + \omega_0 \end{pmatrix}. \tag{2.18}$$

2.5 Power Control in the DQ-Frame

The power controller used in the system equations and simulations is shown in fig. 2.8.

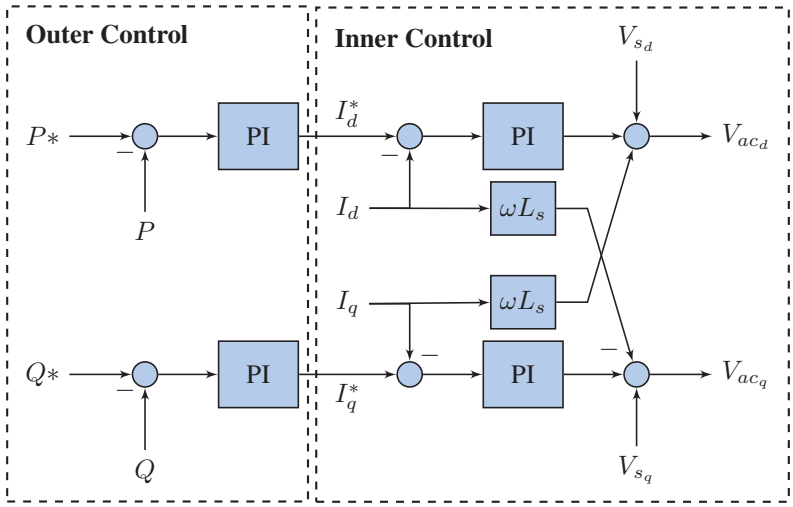

Figure 2.8: Block diagram of the power control structure

The inner control structure in fig. 2.8 regulates the current components in the DQ frame, while the outer loop regulates the active and reactive power flowing through the converter. It is assumed that the control structure regulates V_{ac} directly, due to the average model. The equations for the inner controller can easily be derived from the block diagram and are shown in (2.19).

$$\begin{aligned} V_{ac_{dq}} &= V_{s_{dq}} + \hat{\omega} L_s \begin{bmatrix} I_q \\ I_d \end{bmatrix} + K_{p_{is}}((I^*_{dq} - I_{dq}) + \frac{1}{T_{i_{is}}}\gamma_{is}) \\ \dot{\gamma}_{is} &= I^*_{dq} - I_{dq} \end{aligned} \tag{2.19}$$

2.5.1 Inner Current Control Gains

As shown in [15, 16] it is possible to rewrite (2.3) in the DQ frame as (2.20).

$$V_{s_d} - V_{ac_d} = L_s \frac{dI_d}{dt} + R_s I_d - \omega L_s I_q \tag{2.20a}$$

$$V_{s_q} - V_{ac_q} = L_s \frac{dI_q}{dt} + R_s I_q + \omega L_s I_d \tag{2.20b}$$

Inserting (2.19) for V_{ac_d} and V_{ac_q} respectively in (2.20) and differentiating once, we obtain (2.21). It is assumed that $\hat{\omega} \approx \omega$.

$$L_s \frac{d^2 I_{dq}}{dt^2} = K_{p_{is}} \left(\frac{d(I^*_{dq} - I_{dq})}{dt} + \frac{1}{T_{i_{is}}} (I^*_{dq} - I_{dq}) \right) - R_s \frac{dI_{dq}}{dt} \tag{2.21}$$

Assuming that the reference current I^*_{dq} is varying slowly, $\dot{I}^*_{dq} \approx 0$ and we can find the error dynamics $e_{I_{dq}} = I^*_{dq} - I_{dq}$ for the closed loop system as (2.22).

$$\ddot{e}_{I_{dq}} + \frac{K_{p_{is}} + R_s}{L_s} \dot{e}_{I_{dq}} + \frac{K_{p_{is}}}{T_{i_{is}} L_s} e_{I_{dq}} = 0 \tag{2.22}$$

Eq. (2.22) is easily recognized as a second order system and the equations for the PI-controller gains are derived as

$$K_{p_{is}} = \omega^2_{n_{is}} T_{i_{is}} L_s, \qquad T_{i_{is}} = \frac{2\zeta_{is}}{\omega_{n_{is}}} - \frac{R_s}{L_s \omega^2_{n_{is}}}, \tag{2.23}$$

where ω_n and ζ are the natural frequency and damping coefficient of the closed loop.

2.5.2 Outer Power Control Gains

As the thesis objective is to study the effects of the PLL on the entire converter system, and mainly the active power output, it is not necessary to utilize advanced methods for tuning the power controllers. For the reactive power control, I_q is set to zero. For the active power control, we assume that the inner current loop is sufficiently fast, such that the current at the terminal is directly controlled by the inner controller. In addition V_d is assumed constant and $V_q = 0$. With this, the only variable affecting the active power at PCC is I_d, and the open-loop transfer function through the active power controller and the RL-filter can be found as

$$K_{p_p} \left(\frac{1 + T_{i_p} s}{T_{i_p} s} \right) \frac{1}{R_s + L_s s}. \tag{2.24}$$

The natural frequency and damping coefficient are found from the denominator of the closed-loop transfer function. The resulting expression for the controller gains are

$$K_{p_p} = \omega^2_{n_p} T_{i_p} L_s, \qquad T_{i_p} = \frac{2\zeta_p}{\omega_{n_p}} - \frac{R_s}{L_s \omega^2_{n_p}}. \tag{2.25}$$

2.6 Non-Linear Stability for Autonomous Systems

Stability conditions for a system of linear ordinary differential equations are easy to formulate. Due to its linearity, a system on the form

$$\dot{x} = Ax \tag{2.26}$$

have only one equilibrium point, and its global stability properties are derived from the eigenvalues of the matrix A. For an autonomous non-linear system on the form

$$\dot{x} = f(x) \tag{2.27}$$

reaching a conclusion about global stability is not always easy. A common starting point for non-linear stability analysis, is finding the local properties at each equilibria (as the non-linear system can have more than one) by linearising the equations about the respective points and study the corresponding eigenvalues [17]. This analysis gives an indication about the behaviour in the immediate neighbourhood of each point, but is unable to tell us anything about the size of the neighbourhood, and thus the global properties of the system. To make a global stability conclusion we can apply the tools developed by the Russian mathematician Alexandr Lyapunov.

For the system (2.27) with an equilibrium point at $x = 0$, $D \subset \mathbb{R}^n$ containing $x = 0$, we have the following conditions for the Lyapunov function $V(x)$:

$$V(0) = 0, \quad V(x) > 0 \quad \forall x \in D \setminus \{0\}. \tag{2.28}$$

If

$$\dot{V} = \frac{\partial V}{\partial x}\dot{x} = \frac{\partial V}{\partial x} f(x) \leq 0 \quad \forall x \in D \tag{2.29}$$

then $x = 0$ is stable on the domain D. In addition, if

$$\dot{V} < 0 \quad \forall x \in D \setminus \{0\}, \tag{2.30}$$

$x = 0$ is asymptotically stable in D. When $D = \mathbb{R}^n$ we have global asymptotic stability.

3 | Phase-Locked Loops

General phase synchronization systems has for a long time been a topic of interest for researchers. The first mentions of advanced PLL concepts, such as pull-in and hold-in range dates back to 1966 [18], concepts which will be introduced later in this chapter. However, these concepts and definitions have largely gone unnoticed by scientists applying the PLL to power converter systems. Multiple failures observed in voltage source converters are assumed to originate from the PLL [6, 19, 20], but the causes remain elusive. In this chapter it is demonstrated how theory developed for general PLL applications relates to the case of power converters.

3.1 General Terminology

The main objective of a phase-locked loop is to synchronize its output to the input signal. When the two signals are synchronized, we say that they are *locked* or in a *locked state*. The transition from an unlocked state to a locked state is called an acquisition process.

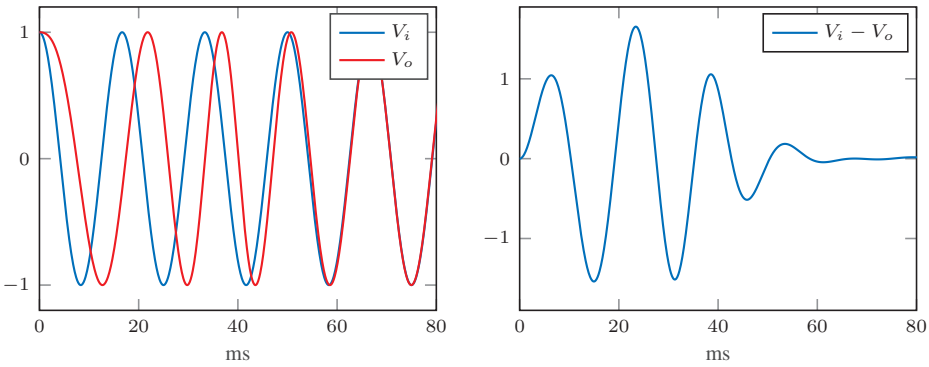

Figure 3.1: Acquisition process with input frequency $f = 60\text{Hz}$, initial frequency $f_0 = 15\text{Hz}$ and loop parameters $\omega_n = 0.43\pi f,\ \zeta = 1$.

Fig. 3.1 present an acquisition process where the output signal V_o is slowly synchronized to the input signal V_i. Near the end of the figure the signals are locked and the difference between them is zero.

A general structure used in mathematical modelling and analysis of the PLL is shown in fig. 3.2.

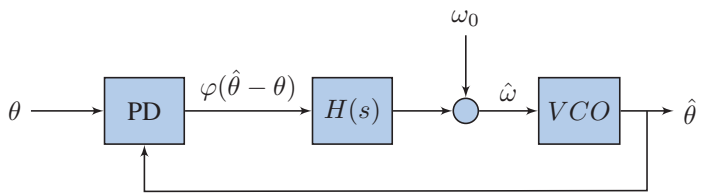

Figure 3.2: General PLL structure

The general function $\varphi(\hat{\theta} - \theta) = \varphi(\theta_\Delta)$, labeled as the phase detector (PD), usually consists of a non-linear trigonometric function such as $\sin(\theta_\Delta)$. However, multiple alternatives is mentioned in [8, 10]. The feedback controller, compensator or loop-filter can be a general transfer function, such as the first order PI-controller used in the SRF-PLL (section 2.4). In convential literature on PLLs, the integrator between estimated frequency and phase angle is called a voltage controlled oscillator (VCO). In applications other than power converters it is common to include a VCO gain ($\dot{\hat{\theta}} = K_{VCO}\hat{\omega}$), which is omitted in this analysis.

In *Hold-in, pull-in, and lock-in ranges of PLL circuits: rigorous mathematical definitions and limitations of classical theory* [8], various important concepts regarding the PLL analysis is defined rigorously. Equation (3.1) shows the locked state of the PLL, with zero frequency error and constant phase difference θ_{eq} between the input and output signals.

$$\theta_\Delta(t) = \theta_{eq} + 2\pi k, \quad \dot{\theta}_\Delta = \omega_\Delta = 0 \tag{3.1}$$

For a PLL with sinusoidal phase detector, such as the SRF-PLL where $\theta_{eq} = 0$, the definition of (3.1) is

$$\theta_\Delta(t) = 2\pi k, \quad \dot{\theta}_\Delta = \omega_\Delta = 0. \tag{3.2}$$

The article [8] defines the hold-in set $\Omega_{hold-in}$, which is the region of frequency error where the PLL can maintain a locked state, assuming the signal is initially synchronized. This is equivalent to the frequency range where a locally stable equilibrium exists. To further substantiate the difficulties of non-linear analysis of the PLL, Leonov G.A. et al.[8] show that the hold-in range can be a set of disjoint intervals for a second order compensator $H(s)$. The pull-in range $\Omega_{pull-in}$ is a subset of the hold-in range, and describes the initial range of frequency deviations from where the PLL is able to lock to a specific frequency. This is the analogue to the local neighbourhood D, defined in section 2.6, where the equilibrium point is asymptotically stable. These two ranges can be used to find the operating range for the PLL and establish from where the system will or will not reach a locked state.

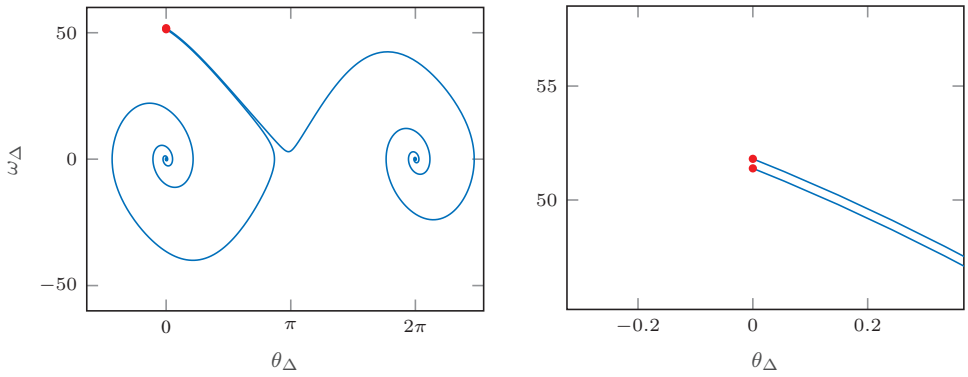

(a) Trajectories from nearly identical conditions leading to different equilibria

(b) Closeup of the initial conditions

Figure 3.3: Cycle slip for a system with sinusoidal PD and PI-control

Seen in fig. 3.3 are two almost identical initial conditions leading to different equilibrium points. During the transient acquisition process, the frequency difference of the upper trajectory reverts back close to the initial ω_Δ, before approaching the stable equilibrium. Increasing the initial frequency difference lead to multiple oscillations and the output of the PLL is not correct. This effect is called cycle slips. The article [8] gives a rigorous mathematical definition for when cycle slips occur (3.3). The initial frequency difference range where no cycle slips arise is defined as the lock-in range $\Omega_{lock-in}$.

$$\limsup_{t\to\infty} \left|\theta_\Delta(0) - \theta_\Delta(t)\right| \geq 2\pi \tag{3.3}$$

For completeness, n cycle slips are defined as

$$\limsup_{t\to\infty} \left|\theta_\Delta(0) - \theta_\Delta(t)\right| \geq 2\pi n, \quad n \in \mathbb{Z}. \tag{3.4}$$

It is believed that a PLL, originally synchronized to the input signal, will experience cycle slips if a step change, larger than the lock-in range, is applied to the input signal frequency. The justification for this assumption is that a infinitely steep step change ω_{step} at $t = T$ can be modelled as the initial condition $\omega_0 = \omega_{step}$ at $t = 0$.

3.2 Linear Analysis of the SRF-PLL

3.2.1 Stability Analysis

A common starting point for any dynamical system analysis, is linear analysis. By examining eigenvalues of the Jacobian near the systems ideal operating point, local stability can be proved. Assuming the phase difference $\hat{\theta} - \theta$ is very small, the small angle approximation (3.5) is valid and can be applied.

$$V_{dq} = \begin{pmatrix} V_s \cos(\hat{\theta} - \theta) \\ -V_s \sin(\hat{\theta} - \theta) \end{pmatrix} \approx \begin{pmatrix} V_s \\ -V_s(\hat{\theta} - \theta) \end{pmatrix} \tag{3.5}$$

The differential equations for the SRF-PLL (2.18) can be rewritten as

$$\begin{pmatrix} \dot{\hat{\theta}} \\ \dot{\hat{\omega}} \end{pmatrix} = \begin{pmatrix} \hat{\omega} \\ -K_p V_s((\hat{\omega} - \omega)\cos(\hat{\theta} - \theta) + \frac{1}{T_i}\sin(\hat{\theta} - \theta)) \end{pmatrix}, \tag{3.6}$$

where ω_0 is considered an initial condition. A constant input frequency ω is assumed, thus the coordinate transformation (3.7) can be applied to (2.18) to obtain the error dynamics (3.8).

$$\begin{pmatrix} \theta_\Delta = \hat{\theta} - \theta \\ \omega_\Delta = \hat{\omega} - \omega \end{pmatrix} \tag{3.7}$$

$$\begin{pmatrix} \dot{\theta_\Delta} \\ \dot{\omega_\Delta} \end{pmatrix} = \begin{pmatrix} \omega_\Delta \\ -K_p V_s(\omega_\Delta \cos(\theta_\Delta) + \frac{1}{T_i}\sin(\theta_\Delta)) \end{pmatrix} \tag{3.8}$$

It is easy to see that the dynamics of the system is invariant to the transformation when ω is constant (3.9).

$$\begin{aligned} \dot{\theta_\Delta} &= \dot{\hat{\theta}} - \dot{\theta} = \hat{\omega} - \omega = \omega_\Delta \\ \dot{\omega_\Delta} &= \dot{\hat{\omega}} - \dot{\omega} = \dot{\hat{\omega}}. \end{aligned} \tag{3.9}$$

Inserting (3.5) in (3.8), (3.10) is obtained.

$$\begin{pmatrix} \dot{\theta_\Delta} \\ \dot{\omega_\Delta} \end{pmatrix} = \begin{pmatrix} \omega_\Delta \\ -K_p V_s(\omega_\Delta + \frac{1}{T_i}\theta_\Delta) \end{pmatrix} \tag{3.10}$$

Eq. (3.10) is equivalent to

$$\begin{pmatrix} \dot{\theta_\Delta} \\ \dot{\omega_\Delta} \end{pmatrix} = A \begin{pmatrix} \theta_\Delta \\ \omega_\Delta \end{pmatrix}, \quad A = \begin{pmatrix} 0 & 1 \\ -\frac{K_p V_s}{T_i} & -K_p V_s \end{pmatrix}. \tag{3.11}$$

To check system stability the characteristic equation

$$|A - \lambda I| = 0 \tag{3.12}$$

is solved and the eigenvalues are

$$\lambda_{1,2} = \frac{1}{2}\left(-K_p V_s \pm \sqrt{(K_p V_s)^2 - 4\frac{K_p V_s}{T_i}}\right). \tag{3.13}$$

From (3.13), condition (3.14) is found, which ensures $\mathrm{Re}(\lambda) < 0$ and exponential stability of the linearised system.

$$-\frac{K_p V_s}{T_i} < 0 \tag{3.14}$$

3.2.2 Controller Gains

Rewriting (3.10) as a linear ordinary differential equation (ODE), the system is easily recognized as a mass-spring-damper system (3.15).

$$\ddot{x} + K_p V_s \dot{x} + \frac{K_p V_s}{T_i} x = 0 \tag{3.15}$$

The equations for natural frequency ω_n and damping ratio ζ are

$$\omega_n = \sqrt{\frac{K_p V_s}{T_i}}, \qquad \zeta = \frac{K_p V_s}{2\omega_n} = \frac{1}{2}\sqrt{K_p V_s T_i}, \tag{3.16}$$

the same result as [21]. Rearranging, the inverse relationship is found, which is useful to obtain a specific transient step response defined by ω_n and ζ (3.17).

$$K_p = \frac{2\zeta\omega_n}{V_s}, \qquad T_i = \frac{2\zeta}{\omega_n} \tag{3.17}$$

As portrayed by fig. 3.4 these control parameters result in fast phase acquisition and little overshoot.

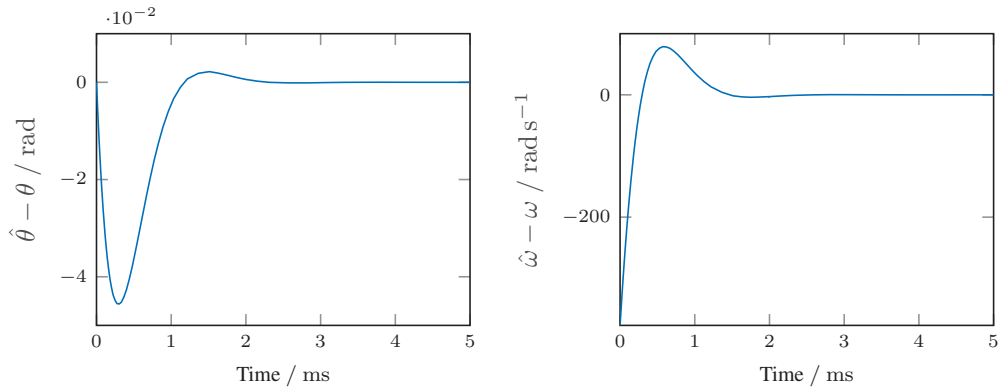

Figure 3.4: Step response showing phase and frequency error with initial conditions $(\theta_0, \omega_0) = 0$ and $\omega_n = 10\omega,\ \omega = 2\pi 60,\ \zeta = 1/\sqrt{2}$.

3.3 Non-Linear Analysis of the SRF-PLL

While we know that the SRF-PLL performs well in its linear operating range, there are certain cases where the PLL exhibits unpredictable behaviour [6]. To understand possible problem sources it is worthwhile to analyze the PLL in the non-linear domain. From this analysis, we can hopefully determine if undesirable behaviour stems from the PLL operating outside its linear range (where the small angle approximation is inaccurate).

3.3.1 Equilibrium Points Classification

We solve the differential equations (3.8) for $\dot{\theta_\Delta} = 0,\ \dot{\omega_\Delta} = 0$ to obtain the equilibrium points of the system (3.18).

$$\theta_\Delta = k\pi :\ k \in \mathbb{Z},\ \omega_\Delta = 0 \tag{3.18}$$

Using the linearisation theorem [22], we can determine the behaviour in the immediate vicinity of each equilibrium point.

$$J = \begin{pmatrix} \frac{\partial f_1}{\partial \theta_\Delta} & \frac{\partial f_1}{\partial \omega_\Delta} \\ \frac{\partial f_2}{\partial \theta_\Delta} & \frac{\partial f_2}{\partial \omega_\Delta} \end{pmatrix} = \begin{pmatrix} 0 & 1 \\ V_s K_p(\omega_\Delta \sin(\theta_\Delta) - \frac{1}{T_i}\cos(\theta_\Delta)) & -V_s K_p \cos(\theta_\Delta) \end{pmatrix} \tag{3.19}$$

For the set of equilibrium points with even k's, the Jacobian has the following entries:

$$J = \begin{pmatrix} 0 & 1 \\ -\frac{V_s K_p}{T_i} & -V_s K_p \end{pmatrix}. \tag{3.20}$$

For odd k's' we have

$$J = \begin{pmatrix} 0 & 1 \\ \frac{V_s K_p}{T_i} & V_s K_p \end{pmatrix}. \tag{3.21}$$

The Jacobian for even k's is identical to the A-matrix from the linearised system (3.11). Assuming condition (3.14) is true, the set of equilibrium points spanned by even k's are stable focus points [17]. The eigenvalues for odd k's are

$$\lambda_{1,2} = \frac{1}{2}\left(V_s K_p \pm \sqrt{(V_s K_p)^2 + 4\frac{V_s K_p}{T_i}}\right). \tag{3.22}$$

Again, assuming (3.14), eigenvalues spanned by odd k's are real with opposite signs. This means that the equilibrium points are saddle points [17]. The stable focus points lead to a correct phase prediction (the equilibrium points are 2π-periodic) and the equilibria giving an incorrect phase prediction (shifted by π), only have two stable trajectories [17]. However, the global domain of attraction for the equilibrium points are not known. For this task we need Lyapunov stability theory.

3.3.2 Global Stability Analysis

The search for Lyapunov candidate functions can be quite time-consuming. Fortunately, [23] lists a candidate function for a PI-controlled PLL with a 2π-periodic phase detector (PD), such as the SRF-PLL. Rewriting (2.18) with a general non-linear phase detector, $\varphi(\hat{\theta} - \theta)$, we find

$$\begin{pmatrix} \dot{\gamma} \\ \dot{\hat{\theta}} \end{pmatrix} = \begin{pmatrix} -V_s \varphi(\hat{\theta} - \theta) \\ K_p(-V_s \varphi(\hat{\theta} - \theta) + \frac{1}{T_i}\gamma) + \omega_0 \end{pmatrix}. \tag{3.23}$$

As before, we assume $\dot{\theta} = \omega$ is a constant input frequency and write the output of the PLL as $\dot{\hat{\theta}} = \hat{\omega} + \omega_0$, where ω_0 is the initial value for the frequency. Using the linear transformation, $\gamma \to -V_s\gamma$, the following differential equations for $\dot{\theta_\Delta} = \dot{\hat{\theta}} - \dot{\theta} = \hat{\omega} + \omega_0 - \omega$ are found:

$$\begin{pmatrix} \dot{\gamma} \\ \dot{\theta_\Delta} \end{pmatrix} = \begin{pmatrix} \varphi(\theta_\Delta) \\ -K_p V_s(\varphi(\theta_\Delta) + \frac{1}{T_i}\gamma) + (\omega_0 - \omega) \end{pmatrix}. \tag{3.24}$$

The Lyapunov candidate function from [23] with slightly modified notation is

$$V(\gamma, \theta_\Delta) = \frac{K_p V_s}{2T_i} \left(\gamma - \frac{T_i}{K_p V_s}(\omega_0 - \omega) \right)^2 + \int_0^{\theta_\Delta} \varphi(s) ds. \tag{3.25}$$

We find the equilibrium points of (3.24) by solving the following equation

$$\begin{pmatrix} 0 \\ 0 \end{pmatrix} = \begin{pmatrix} \varphi(\theta_{\Delta_{eq}}) \\ -K_p V_s \left(\varphi(\theta_{\Delta_{eq}}) + \frac{1}{T_i}\gamma_{eq} \right) \end{pmatrix}, \tag{3.26}$$

and obtain the points

$$\begin{pmatrix} \gamma_{eq} \\ \theta_{\Delta_{eq}} \end{pmatrix} = \begin{pmatrix} k\pi \\ \frac{T_i}{K_p V_s}(\omega_0 - \omega) \end{pmatrix}, \quad k \in \mathbb{Z} \tag{3.27}$$

for a system with a sinusoidal phase detector $\varphi(\theta_\Delta) = \sin(\theta_\Delta)$. The integral of the phase detector is

$$\int_0^{\theta_\Delta} \sin(s) ds = 1 - \cos(\theta_\Delta) > 0 \quad \forall\, \theta_\Delta \neq \theta_{\Delta_{eq}}, \tag{3.28}$$

and we can conclude that the Lyapunov candidate function is positive definite. The time-derivative is

$$\dot{V} = \frac{K_p V_s}{T_i} \left(\gamma - \frac{T_i}{K_p V_s}(\omega_0 - \omega) \right) \dot{\gamma} + \varphi(\theta_\Delta)\dot{\theta_\Delta} = -K_p V_s \varphi^2(\theta_\Delta), \tag{3.29}$$

and as we know that $\varphi(0) = 0$, which implies $\dot{\gamma} = 0$ (LaSalle's invariance principle [17]) and that (3.25) is radially unbounded in γ, we can conclude that the system is globally asymptotically stable. We know from the equilibrium points classification in section 3.3.1 that almost all trajectories tend to the 2π-periodic focus points spanned by even k's, which lead to the correct phase prediction. Only the exceptional case of $\theta_{\Delta_0} = (2k+1)\pi : k \in \mathbb{Z},\ \omega_{\Delta_0} = 0$ and the two stable trajectories belonging to the saddle points, leads to an incorrect phase prediction. All trajectories reach an equilibrium. Thus, ignoring these exceptional cases, we can say that for all practical purposes $\Omega_{hold-in} = \Omega_{pull-in} = \mathbb{R}^2$.

As we can see from fig. 3.5, the solutions approach one of the multiple equilibria, except for the initial points $\theta_\Delta \pm \pi,\ \omega_\Delta = 0$ where $\dot{\theta_\Delta}, \dot{\omega_\Delta} = 0$. The two trajectories escaping the plotted range experience multiple cycle slips and reach equilibrium points further away.

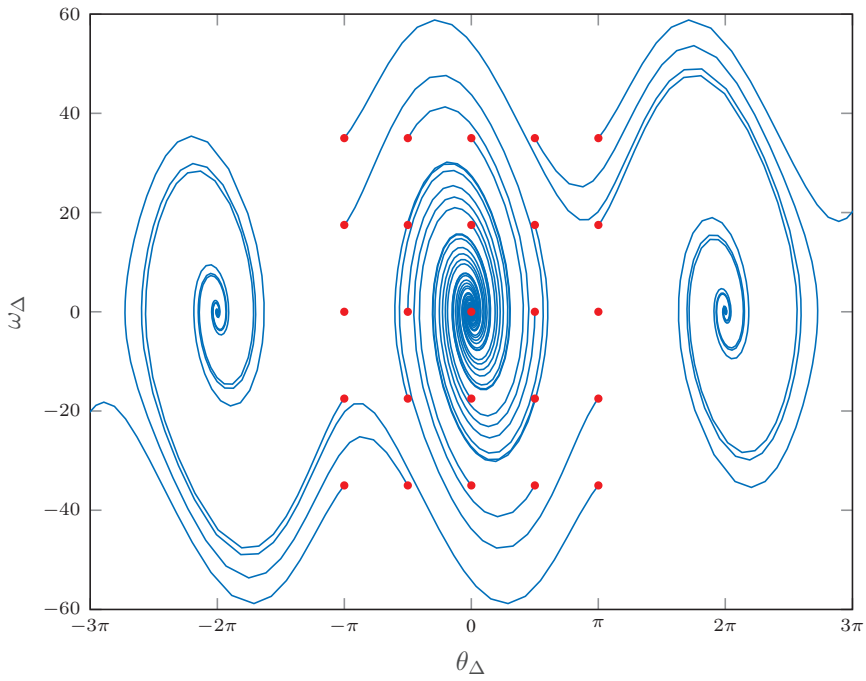

Figure 3.5: Various trajectories of the system (3.8) with the red dots as initial conditions. $K_p = 10,\ T_i = 0.02,\ V_s = 1$, which leads to a very under-damped system.

3.4 Lock-In Range for SRF-PLL

Fig. 3.3a indicates that there exists a boundary separating the trajectories tending to separate equilibria from almost identical initial conditions. Such a boundary is formally known as a separatrix. An analytical estimate is found in the PHD-thesis [23], utilizing a Taylor series expansion. Since notation in [23] differs slightly from this thesis, a summary of the derivation is included for completion.

We introduce the variables $x_1 = \theta_\Delta$ and $x_2 = \omega_\Delta$. The differential equation for the curve $x_2(x_1)$ is written as

$$\frac{dx_2}{dx_1} = \frac{K_p V_s(-\cos(x_1)x_2 - \frac{1}{T_i}\sin(x_1))}{x_2}. \tag{3.30}$$

Following the derivation from [23] we set $x_2 = S(x_1) \implies dx_2 = dS(x_1)$, where S is the separatrix we want to find.

$$S(x_1)dS(x_1) = (K_p V_s(-\cos(x_1)S(x_1) - \frac{1}{T_i}\sin(x_1)))dx_1 \tag{3.31}$$

Integrating both sides on the interval $[0, \pi)$ yields

$$\begin{aligned}\int_{x_1}^{\pi} S(\zeta)dS(\zeta) &= -K_p V_s \int_{x_1}^{\pi} \cos(\zeta)S(\zeta)d\zeta - \frac{K_p V_s}{T_i}\int_{x_1}^{\pi}\sin(\zeta)d\zeta \\ \frac{1}{2}\lim_{\zeta\to\pi^-} S^2(\zeta) - \frac{1}{2}S^2(x_1) &= -K_p V_s \int_{x_1}^{\pi} \cos(\zeta)S(\zeta)d\zeta - \frac{K_p V_s}{T_i}(1+\cos(x_1)).\end{aligned} \tag{3.32}$$

Approaching from the left we find

$$\frac{1}{2}\lim_{\zeta\to\pi^-} S^2(\zeta) = 0, \tag{3.33}$$

which gives

$$-\frac{1}{2}S^2(x_1) = -K_p V_s \int_{x_1}^{\pi} \cos(\zeta)S(\zeta)d\zeta - \frac{K_p V_s}{T_i}(1+\cos(x_1)). \tag{3.34}$$

Now, the trick is to expand the separatrix $S(x_1)$ as a Taylor series, **not** in x_1, but in $a = K_p$ in the neighbourhood of $K_p = 0$.

$$\begin{aligned}S(x_1, a) &= S(x_1, 0) + a\frac{\partial S}{\partial a}\bigg|_{a=0} + \frac{a^2}{2!}\frac{\partial^2 S}{\partial a^2}\bigg|_{a=0} + ... \\ &= S_0(x_1, 0) + S_1(x_1)a + S_2(x_1)a^2 + ...\end{aligned} \tag{3.35}$$

Inserting in the original equation gives

$$\begin{aligned}-\frac{1}{2}(S_0(x_1,0) + S_1(x_1)a + S_2(x_1)a^2 + ...)^2 &= -aV_s\int_{x_1}^{\pi}\cos(\zeta)(S_0(x_1,0) \\ +S_1(x_1)a + S_2(x_1)a^2 + ...)d\zeta &- \frac{K_p V_s}{T_i}(1+\cos(x_1)).\end{aligned} \tag{3.36}$$

Now, by comparing the terms of equal exponent it is possible to find an analytical approximation for the separatrix.

$$\frac{1}{2}(S_0(x_1,0))^2 = \frac{K_p V_s}{T_i}(1+\cos(x_1)) \tag{3.37}$$

$$(S_0(x_1,0)S_1(x_1))a = aV_s\int_{x_1}^{\pi}\cos(\zeta)(S_0(\zeta,0)d\zeta \tag{3.38}$$

$$(S_0(x_1,0)S_2(x_1)+S_2(x_1)^2)a^2 = a^2V_s\int_{x_1}^{\pi}\cos(\zeta)(S_1(\zeta)d\zeta \tag{3.39}$$

These integrals are solved in [23] and the resulting formula for the separatrix $S(x_1, K_p)$ is:

$$\begin{aligned} S(x_1, a=K_p) = &\sqrt{\frac{K_pV_s}{T_i}(1+\cos(x_1))} + \frac{V_s(\frac{2}{3}-\sin(\frac{x_1}{2})-\frac{1}{3}\sin(\frac{3x_1}{2}))}{\cos(\frac{x_1}{2})}K_p \\ &+\frac{V_s^2}{6\sqrt{\frac{K_pV_s}{T_i}\cos(\frac{x_1}{2})}}\left(6.5-4\ln 2-8\sin(\frac{x_1}{2})-4\ln\left|\sin(\frac{x_1}{2})+1\right|\right. \\ &\left.+\frac{1}{2}\cos(2x_1)+2\cos(x_1)\right)K_p^2 - V_s^2\left(\frac{\frac{2}{3}-\sin(\frac{x_1}{2})-\frac{1}{3}\sin(\frac{3x_1}{2})}{4\sqrt{\frac{K_pV_s}{T_i}\cos^3(\frac{x_1}{2})}}\right)K_p^2. \end{aligned} \tag{3.40}$$

The first and second approximation of (3.40) are used to calculate the initial conditions for fig. 3.3. The figure shows that the first estimate presumably gives an upper bound on the region where cycle slips will not occur.

3.5 Special Considerations for Orthogonal Signal Creation

A key assumption for generating the orthogonal signals with a time delay (explained in section 2.3.3) is knowledge of the exact grid frequency. This is quite the contradiction, knowing that the purpose of the PLL is to estimate the unknown grid frequency. Numerous attempts have been made to solve this issue, with the most popular solution being the second order generalized integrator (SOGI)-PLL [24]. The SOGI-PLL introduces feedback of the estimated frequency from the PLL to the orthogonal signal construction. This however, creates a new feedback loop with altered closed loop dynamics. For the purpose of investigating stability and non-linear behaviour in the PLL, the SOGI is omitted due to the increase in complexity. In this section a model for the time-delay based SRF-PLL is derived and analysed to investigate how the stability properties of the system change when there is a difference between assumed grid frequency and true frequency.

To construct the orthogonal voltage signal, V_β, a phase delay of $\frac{\pi}{2}$ is applied. In the time domain, this translates to a delay by a quarter of a full cycle (3.41), where f_0 is the assumed grid frequency.

$$T = \frac{1}{4f_0} \tag{3.41}$$

The Laplace transform of a time delayed signal is

$$\mathscr{L}\{f(t-T)\} = e^{-Ts}F(s). \tag{3.42}$$

Setting $s = j\omega$, the frequency domain representation of the time delay is $e^{-j\omega T}$. The phase of the time delay is then found as

$$\angle e^{-j\omega T} = \arctan\left(-\frac{\sin(\omega T)}{\cos(\omega T)}\right) = -\omega T. \tag{3.43}$$

Inserting (3.41), the phase of the delayed signal is

$$-\omega\frac{1}{4f_o} = -\frac{\omega}{\omega_0}\frac{\pi}{2}. \tag{3.44}$$

With (3.44) we can model the case where the grid frequency is not exactly known (3.45). It is assumed that $\frac{\omega}{\omega_0} \in (0, 2)$.

$$V_{\alpha\beta} = \begin{pmatrix} V_s\cos(\omega t) \\ V_s\cos(\omega t - \frac{\omega}{\omega_0}\frac{\pi}{2}) \end{pmatrix} \tag{3.45}$$

3.5.1 Expanded PLL State Model

Inserting (3.45) in the DQ transform yields

$$V_{dq} = \begin{pmatrix} \cos(\hat{\theta})\cos(\omega t) + \sin(\hat{\theta})\cos(\omega t - \frac{\omega}{\omega_0}\frac{\pi}{2}) \\ -\sin(\hat{\theta})\cos(\omega t) + \cos(\hat{\theta})\cos(\omega t - \frac{\omega}{\omega_0}\frac{\pi}{2}) \end{pmatrix}. \tag{3.46}$$

With $\omega t = \theta$, V_q is found as

$$V_q = \frac{V_s}{2}\left(-\sin(\hat{\theta}-\theta) - \sin(\hat{\theta}+\theta) + \cos(\hat{\theta}-\theta+\frac{\omega}{\omega_0}\frac{\pi}{2}) + \cos(\hat{\theta}+\theta-\frac{\omega}{\omega_0}\frac{\pi}{2})\right).$$

Introducing the variables

$$\begin{aligned} x_1 &= \hat{\theta} - \theta \\ x_2 &= \hat{\theta} + \theta, \end{aligned} \tag{3.47}$$

we get

$$V_q = \frac{V_s}{2}\left(-\sin(x_1) - \sin(x_2) + \cos(x_1 + \frac{\omega}{\omega_0}\frac{\pi}{2}) + \cos(x_2 - \frac{\omega}{\omega_0}\frac{\pi}{2})\right).$$

The differential equations for the expanded PLL system is then

$$\begin{aligned} \dot{\gamma} &= \varphi(x_1, x_2) \\ \dot{x_1} = \hat{\omega} - \omega &= -K_p V_s(\varphi(x_1, x_2) + \frac{1}{T_i}\gamma) + (\omega_0 - \omega) \\ \dot{x_2} = \hat{\omega} + \omega &= -K_p V_s(\varphi(x_1, x_2) + \frac{1}{T_i}\gamma) + (\omega_0 + \omega), \end{aligned} \tag{3.48}$$

with φ as

$$\varphi(x_1, x_2) = \frac{1}{2}\left(\sin(x_1) + \sin(x_2) - \cos(x_1 + \frac{\omega}{\omega_0}\frac{\pi}{2}) - \cos(x_2 - \frac{\omega}{\omega_0}\frac{\pi}{2})\right).$$

3.5.2 Local Stability Analysis

Solutions for the equilibria of the system are found by setting the derivates $\dot{\gamma},\ \dot{x_1}$ to zero. The variable x_2 is expected to be continuously increasing and having a non-zero time-derivate.

$$\begin{aligned} \dot{\gamma} = 0 \implies \varphi(x_1, x_2) &= 0 \\ \dot{x_1} = 0 \implies \gamma_{eq} &= \frac{T_i}{K_p V_s}(\omega_0 - \omega) \\ \dot{x_2} = -K_p V_s\left(\frac{1}{T_i}\gamma_{eq}\right) + (\omega_0 + \omega) \implies x_{2_{eq}} &= 2\int_0^t \omega dt = 2\omega t \stackrel{\text{def}}{=} 2\theta \end{aligned} \tag{3.49}$$

The solution for $x_{1_{eq}}$ is found by setting $\varphi(x_1, 2\theta) = 0$ and solved with the symbolic computing toolbox *Maple*. Similar to the case where the grid frequency is known, $x_{1_{eq}}$ take on values near $x_1 = 0$ and $x_1 = \pi$. The full expression near $x_1 = 0$ can be found in (A.3). A comparison between the analytical expression for $x_{1_{eq}}$ near zero and a numerical simulation of (3.48) is presented in fig. 3.6. The figure shows good agreement between the analytical expression and the numerically obtained solution. The differences in amplitude can probably be attributed to numerical errors.

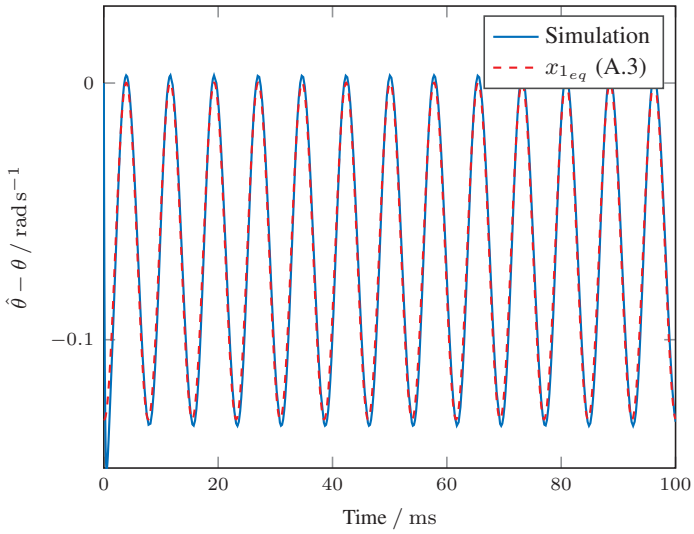

Figure 3.6: Comparison between analytical expression for $x_{1_{eq}}$ and numerical solution with $\omega_0 = 2\pi 60$ and $\omega = 2\pi 65$. $\zeta = 1$ and $\omega_n = 2\omega$ as PLL parameters.

The Jacobian matrix for (3.48) is

$$J = \begin{pmatrix} 0 & \frac{\partial \varphi}{\partial x_1} & \frac{\partial \varphi}{\partial x_2} \\ -\frac{K_p V_s}{T_i} & -K_p V_s \frac{\partial \varphi}{\partial x_1} & -K_p V_s \frac{\partial \varphi}{\partial x_2} \\ -\frac{K_p V_s}{T_i} & -K_p V_s \frac{\partial \varphi}{\partial x_1} & -K_p V_s \frac{\partial \varphi}{\partial x_2} \end{pmatrix}, \tag{3.50}$$

and the corresponding determinant of $J - \lambda I$ is

$$\begin{aligned} |J - \lambda I| = -\lambda \Bigg(\lambda^2 + K_p V_s \left(1 + \frac{K_p V_s}{T_i}\right) \left(\frac{\partial \varphi}{\partial x_1} + \frac{\partial \varphi}{\partial x_2}\right) \lambda \\ + (K_p V_s)^2 \frac{\partial \varphi}{\partial x_1} \frac{\partial \varphi}{\partial x_2} \left(1 - \frac{1}{T_i}\right) \Bigg), \end{aligned} \tag{3.51}$$

where one eigenvalue is zero, thus rendering the linear stability analysis inconclusive.

3.5.3 Global Stability Analysis

Reusing the Lyapunov function from [9] (3.25) with the system (3.48) yields a negative semi-definite time-derivate everywhere, except at the equilibrium. However, the Lyapunov function is not easy to prove positive definite everywhere (3.52). The terms multiplied by x_1 will vanish quickly, the integral of the PD will be zero and γ^2 will dominate, but it is

hard to prove $V(x) > 0 \; \forall \; x \neq 0$ mathematically. The computing toolbox *Maple* did not give a definite answer either.

$$\begin{aligned} V(\gamma, x_1, x_2) &= \frac{K_p V_s}{2T_i}\left(\gamma - \frac{T_i}{2K_p V_s}(\omega_0 - \omega)\right)^2 + \int_0^{x_1} \varphi(s, x_2) ds \\ &= \frac{K_p V_s}{2T_i}\left(\gamma - \frac{T_i}{2K_p V_s}(\omega_0 - \omega)\right)^2 + \frac{1}{2}\left(-\cos(x_1) + \sin(x_2)x_1\right. \\ &\quad \left. - \sin(x_1 + \frac{\omega}{\omega_0}\frac{\pi}{2}) - \cos(x_2 - \frac{\omega}{\omega_0}\frac{\pi}{2})x_1 + 1 + \sin(\frac{\omega}{\omega_0}\frac{\pi}{2})\right) \end{aligned} \tag{3.52}$$

3.5.3.1 Simulations Indicating Global Stabilty

Fig. 3.7 shows the PLL reaching the equilibrium point for a range of initial phase differences, even when the Lyapunov function is not positive. This indicates that the system might be globally stable, or at least that a better suited Lyapunov function exists. As the search for Lyapunov functions is known to be frustrating and time-consuming, this analysis is not pursued further. For the remainder of the thesis the PLL is assumed globally stable when the true grid frequency is in the immediate vicinity of the assumed frequency.

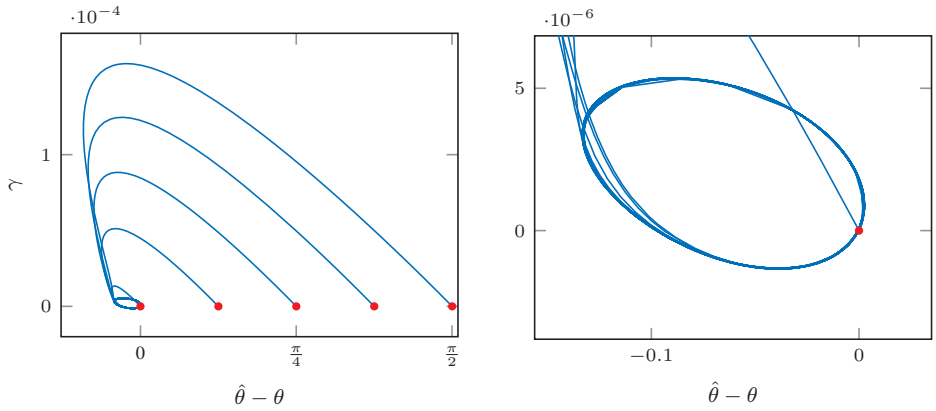

Figure 3.7: Phase plot with $\omega_0 = 2\pi 60$, $\omega = 2\pi 65$, $\zeta = 1$ and $\omega_n = 2\omega$. The plot to the right is a close-up of the orbit in the leftmost plot.

Fig. 3.8a shows that cycle slips are present in the altered system equations as well. The estimated initial frequency difference for when cycle slips occur, the lock in range (3.40), is found to be 2641 $\mathrm{rad\,s^{-1}}$ from the equation and 2602 $\mathrm{rad\,s^{-1}}$ from simulation of the altered system (3.48). This is well within the range of uncertainty and the SRF-PLL with time-delay can be said to exhibit very similar behaviour to the SRF-PLL under ideal conditions, even when the exact grid frequency is not known.

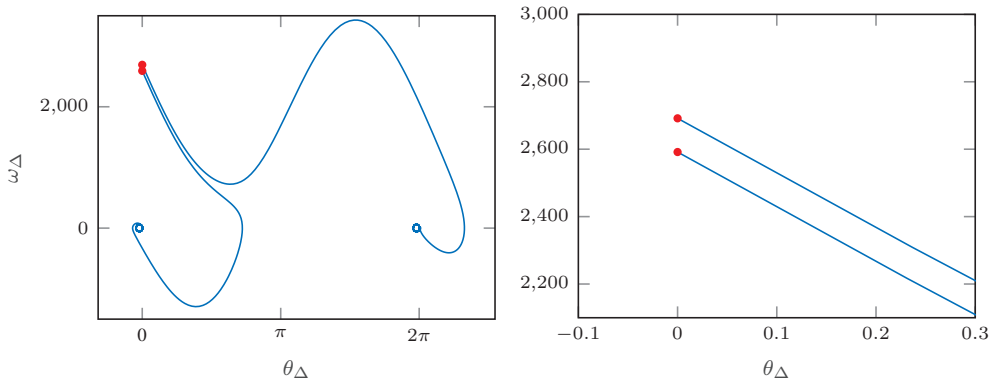

(a) Trajectories from nearly identical conditions leading to different equilibria

(b) Close-up of the initial conditions

Figure 3.8: Cycle slip induced in the system (3.48). $\omega_0 = 2\pi 60$, $\omega = 2\pi 65$, $\zeta = 1$ $\omega_n = 2\omega$.

4 | Results

To investigate possible failure of the PLL, numerous simulations have been performed. Section 4.1 shows the results of simulations intended to verify that the implemented VSC model worked correctly. The results in section 4.2 display how what is believed to be cycle slipping in the PLL can arise and lead to instability in the entire converter system.

All simulations were carried out in the numerical toolbox *Simulink*, using a fixed step solver for the model with switching devices and PWM signals. The step-size was ensured to be less than half the frequency of the carrier wave in the PWM signal generation. The average model was solved with an automatically selected variable step solver, with maximum step-size less than half of the natural frequency of the PLL (which is the fastest loop in the system). When the converter was brought to instability, the average model diverged very fast, thus it is stopped prematurely in some simulations. The parameters used are shown in table 4.1 unless otherwise specified.

Parameter	Symbol	Value	Unit
AC Grid Peak Voltage	V_s	120	V
AC Grid Frequency	f_{grid}	60	Hz
AC Grid Line Resistance	R_{grid}	0.15	Ω
AC Grid Line Inductance	L_{grid}	2	mH
DC Grid Voltage	V_{dc}	200	V
VSC Filter Resistance	R_s	0.15	Ω
VSC Filter Inductance	L_s	12	mH
PLL Time Constant (4τ)	Tr_{pll}	5	ms
PLL Damping Ratio	ζ_{pll}	0.7	-
Current Control Time Constant (4τ)	Tr_{is}	15	ms
Current Control Damping Ratio	ζ_{is}	1.15	-
Active Power Control Time Constant (4τ)	Tr_p	50	ms
Active Power Control Damping Ratio	ζ_p	0.8	-
Current Saturation Limit	-	50	A

Table 4.1: Parameters used in simulations unless otherwise specified

In some of the simulations the VSC is connected to a *weak grid*. The terms *weak grid* and *stiff grid* lack rigorous definition. However, as mentioned in [6], when the impedance of

the grid transmission line is increased, the grid is *weaker*. Therefore, the parameters for grid resistance and inductance has been selected partially by trial and error.

4.1 VSC Model Verification

To verify that the VSC model behaved correctly, a step response simulation was performed. First, the reference of the active power controller was set to 1000 W, then reduced to -1000 W at $t = 1$ s. Fig. 4.1 illustrates that the model works as expected, both for the average and switching device model. No transmission line dynamics were added, thus the measured voltage at PCC was identical to the actual grid voltage.

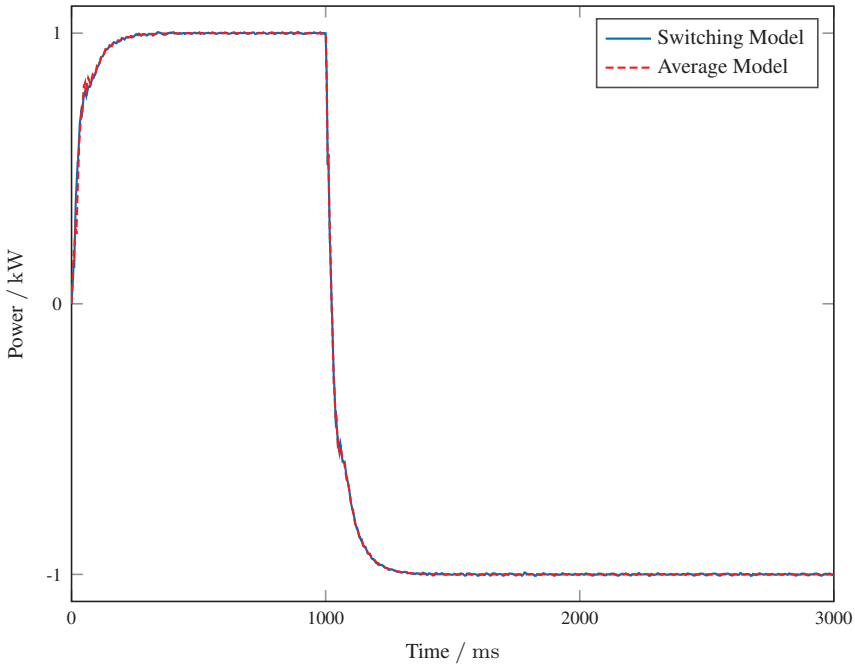

Figure 4.1: Comparison between average and switching device model with steps in active power reference

In fig. 4.2 we see that the PLL reaches a locked state within 10 ms. The average and switching device model show good agreement.

Fig. 4.3 display $\hat{\theta}$ and $\hat{\omega}$ at $t = 1$ s where the active power reference is reduced. The step does not seem to influence the estimated phase and frequency.

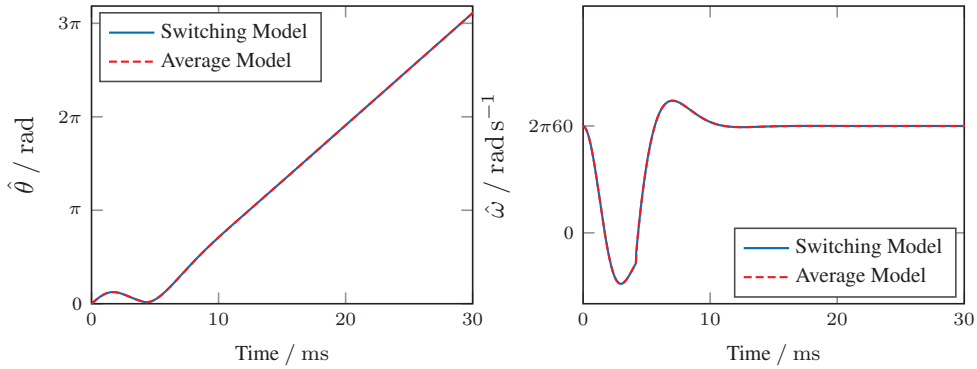

(a) Estimated phase angle **(b)** Estimated frequency

Figure 4.2: Comparison of PLL transient behaviour during acquisition process

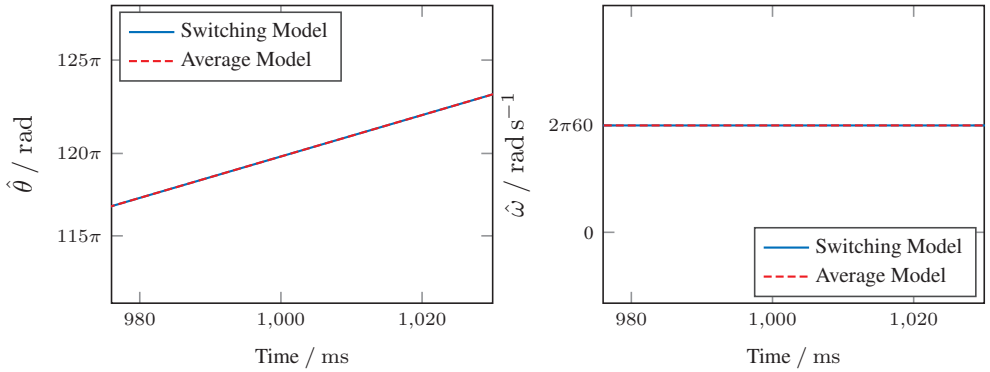

(a) Estimated phase angle **(b)** Estimated frequency

Figure 4.3: Comparison of PLL output at power step change

4.1.1 VSC Connected to Grid

The model was also simulated with a transmission line modelled as a resistor and an inductor in series (portrayed by fig. 2.1). The same step as in fig. 4.1 was applied. Fig. 4.4 shows the resulting active power output of the converter. As the converter output settles at -1000 W, increased oscillation can be seen in the switching device model.

As demonstrated by fig. 4.5, the PLL still acquires lock within 10 ms, and the estimated phase angle indicates strong agreement between the average and switching device model. The estimated frequency behaves similarly for the two models, but the switching device model contains stationary high-frequency oscillations during both the transient and steady state period. This can most likely be attributed to high-frequency components originating in the transistor devices.

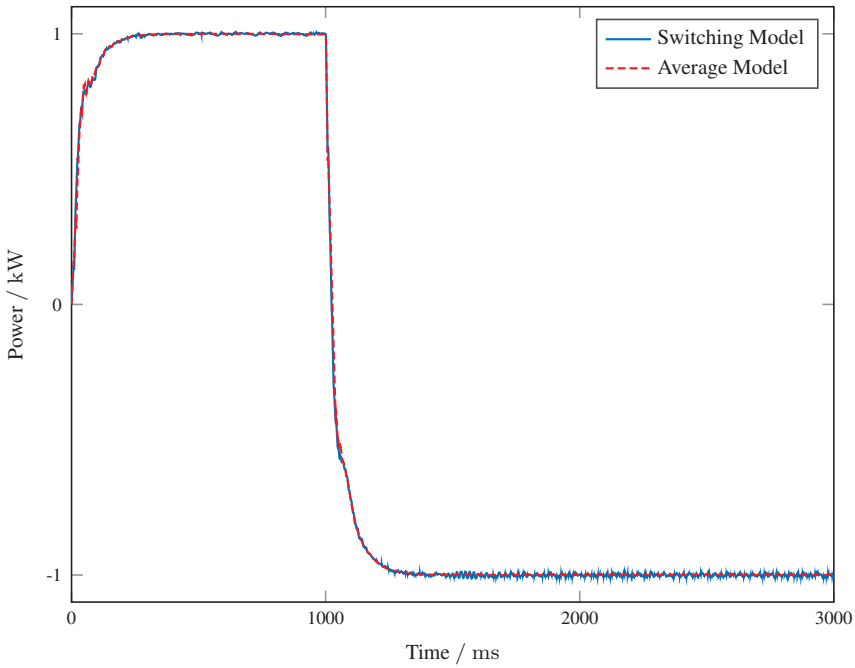

Figure 4.4: Comparison between models with grid connection

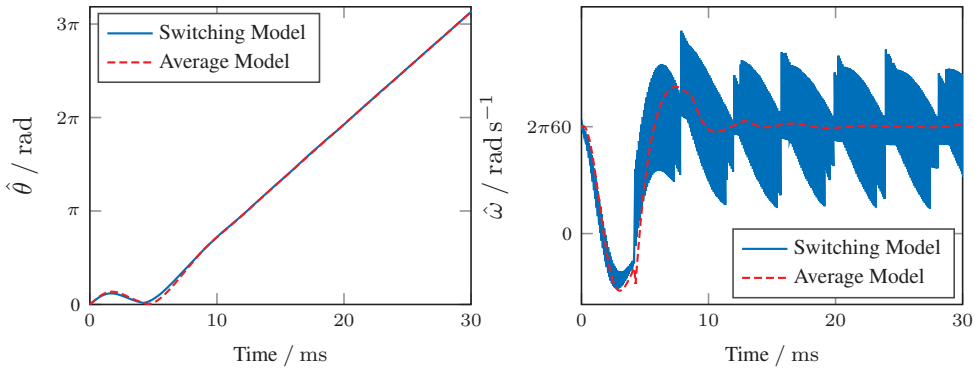

(a) Estimated phase angle

(b) Estimated frequency

Figure 4.5: Comparison of PLL transient behaviour during acquisition process with grid connection

When the large reduction in power is applied, an observable effect is seen in $\hat{\omega}$, demonstrated by fig. 4.6b. The oscillation is seen clearly in the average model. In the switching device model, a change in the envelope of the high-frequency stationary oscillations is observed. As shown in fig. 4.6a, the effect does not influence $\hat{\theta}$ significantly.

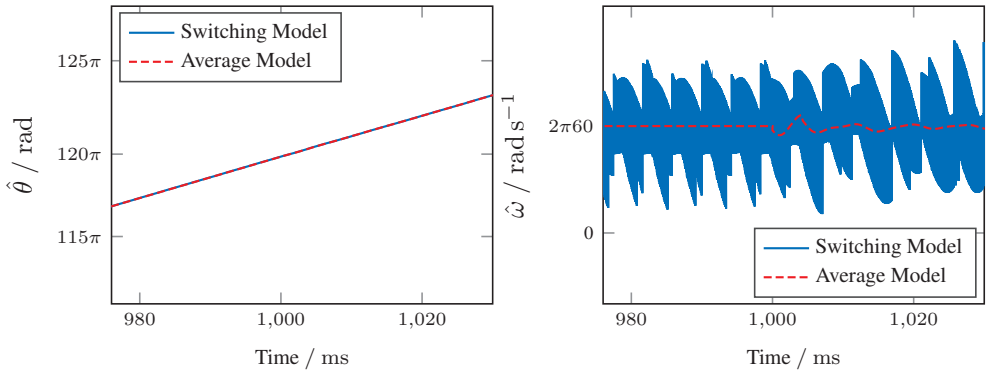

(a) Estimated phase angle

(b) Estimated frequency

Figure 4.6: Comparison of PLL output at power step change with grid connection

4.2 Non-Linear Behaviour in the PLL

4.2.1 Intentionally Provoked Cycle Slips

To demonstrate the effects of non-linear behaviour in the PLL on the entire system, both the average and switching device model was subjected to a frequency disturbance applied internally in the PLL at $t = 1$ s. In these simulations the grid transmission line was not included. Three frequency disturbances were applied to ω_0 (fig. 2.7), the lower and upper estimates from (3.40) and 1.5 times the upper estimate. In fig. 4.7 we see how the average model is very sensitive when the VSC is brought close to instability. In all cases the converter is able to regain steady state after various degrees of transient instability.

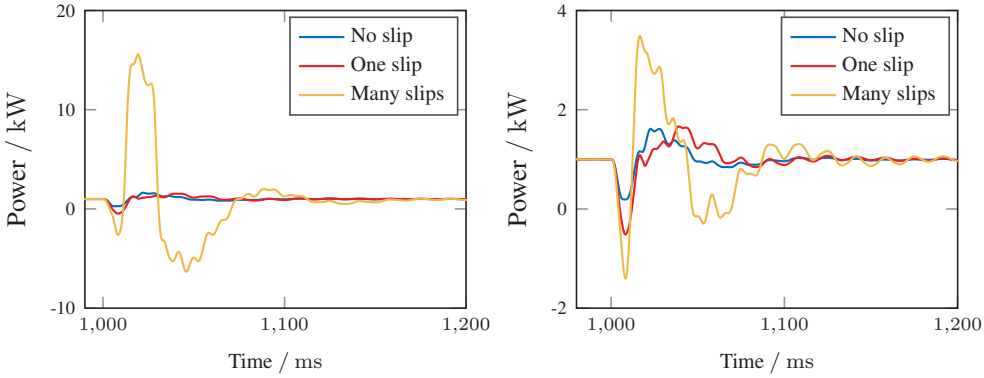

(a) Average model **(b)** Switching device model

Figure 4.7: Comparison of active power output for the two models exposed to cycle slips

Figs. 4.8 and 4.9 show that the PLL is unaffected by the sensitive average model and good agreement between the two models. Recurring oscillations in $\hat{\omega}$ is seen in fig. 4.9 when the PLL experiences more than one cycle slip. These oscillations are seen as small ripples in the phase estimate, $\hat{\theta}$ (fig. 4.8), between $t = 1000\text{ms}$ and $t \approx 1010\text{ms}$.

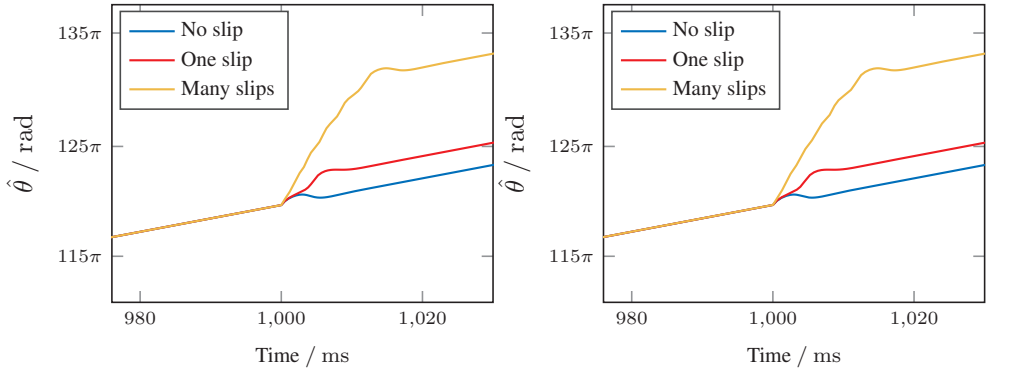

(a) Average model **(b)** Switching device model

Figure 4.8: Comparison of estimated phase angle for the two models exposed to cycle slips

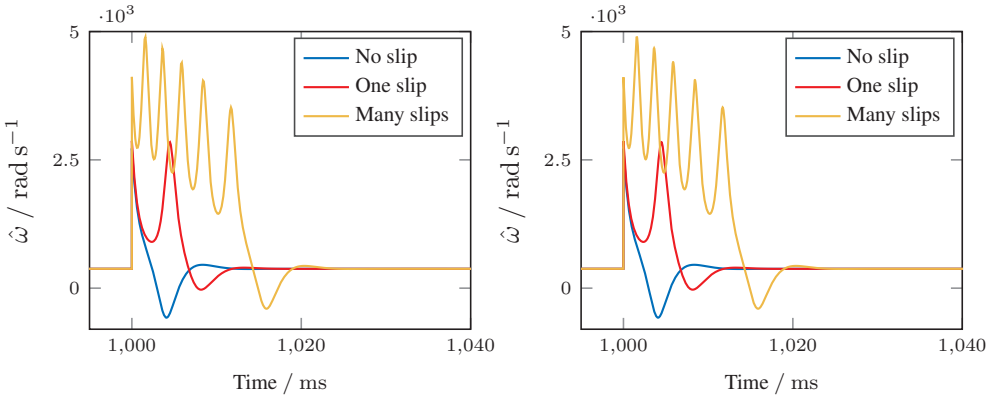

(a) Average model **(b)** Switching device model

Figure 4.9: Comparison of estimated frequency for the two models exposed to cycle slips

In fig. 4.10 phase plots have been constructed for the frequency and phase errors. The true frequency is set according to table 4.1, and the corresponding true phase angle is obtained by integrating the frequency with zero initial condition. The green circles in figs. 4.10a and 4.10b are the initial starting points, the red squares are phase and frequency errors at simulation stop. The phase-plots show good agreement with theoretical results from section 3.4 as the lower estimate of (3.40) lead to zero slips, the upper lead to one slip and 1.5 times the upper estimate lead to numerous (five) slips.

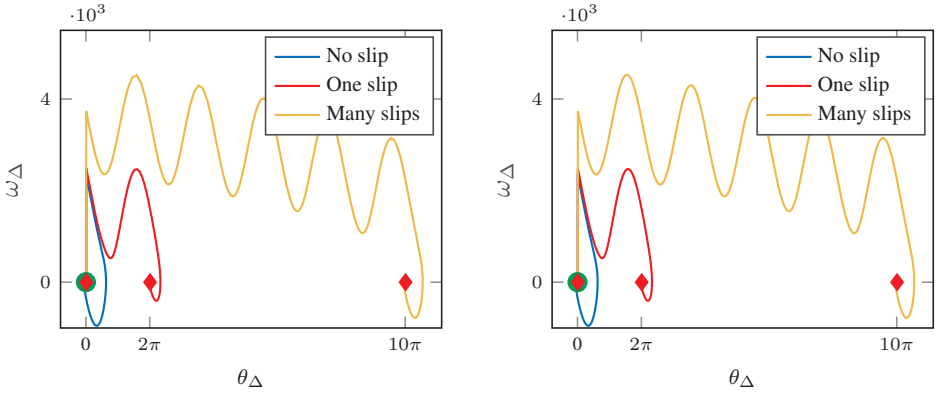

(a) Average model **(b)** Switching device model

Figure 4.10: Phase plot exhibiting the leap from one equilibrium to another

4.2.2 Phase Shift in Grid Source

To see if the PLL can lose track of the phase angle when subjected to grid errors, a phase shift of $\pi/2$ was applied at $t = 1\,\mathrm{s}$ to the grid voltage source V_g. The grid transmission line was included. The line inductance was increased to $8\,\mathrm{mH}$ in the average model simulation and $9\,\mathrm{mH}$ in the switching device simulation. Fig. 4.11 displays the active power output of the converter and the resulting instability from the phase shift. As the average model was solved with a variable-step solver, the step-size approaches zero at the point of instability and was consequently stopped early. The simulations were re-run with a fixed-step solver to see if this would solve the problem, but the fixed-step solver was unable to stay within the (quite large) error tolerances. The fixed-step solver used to solve the switching device model was able to stay within an acceptable error tolerance.

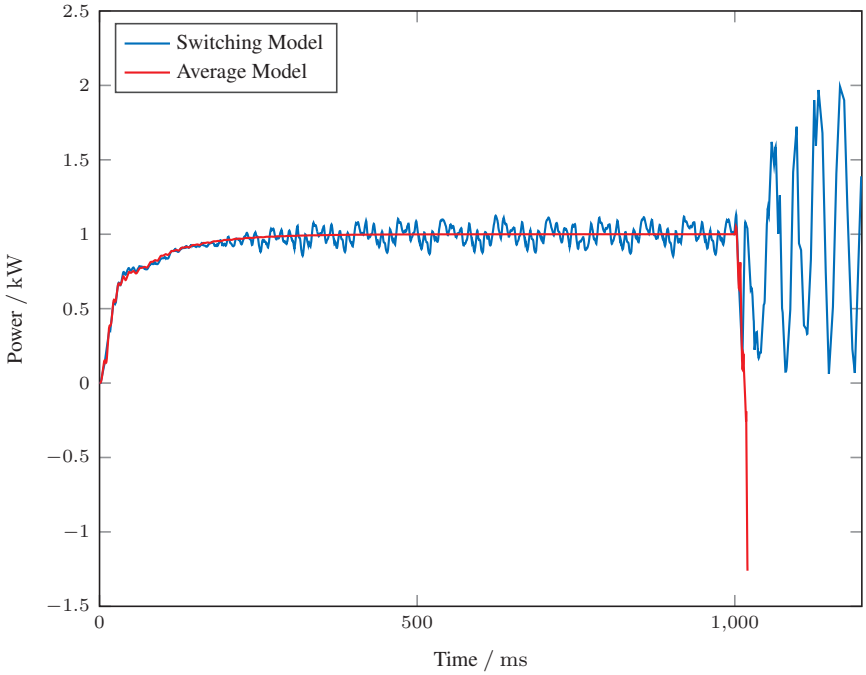

Figure 4.11: Effect of phase shift in grid source on active power output with weak grid connection

The estimated phase and frequency, $\hat{\theta}$ and $\hat{\omega}$, are shown in fig. 4.12. Both models show similar behaviour until the point where the average model diverges. As seen in the frequency estimate (fig. 4.12b) the envelope curve is nearly identical for the first two oscillations. At $t \approx 1010\mathrm{ms}$ in the average model simulation, what is believed to be cycle slipping is shown in fig. 4.13a. The PLL does seem to regain stability at $\theta_\Delta = -2\pi$, as multiple oscillations orbiting this point is observed. However, the large amplitude of the frequency estimate is probably the reason why the model continues to diverge. Cycle slips

are believed to be observed in the switching device model as well (fig. 4.13b), but oscillations from the rapidly switching transistor elements are assumed to pollute the signal significantly. It is not believed that the system regains stability in the vicinity of $\theta_\Delta = 8\pi$, instead it is most likely just a coincidence that the simulation was stopped there.

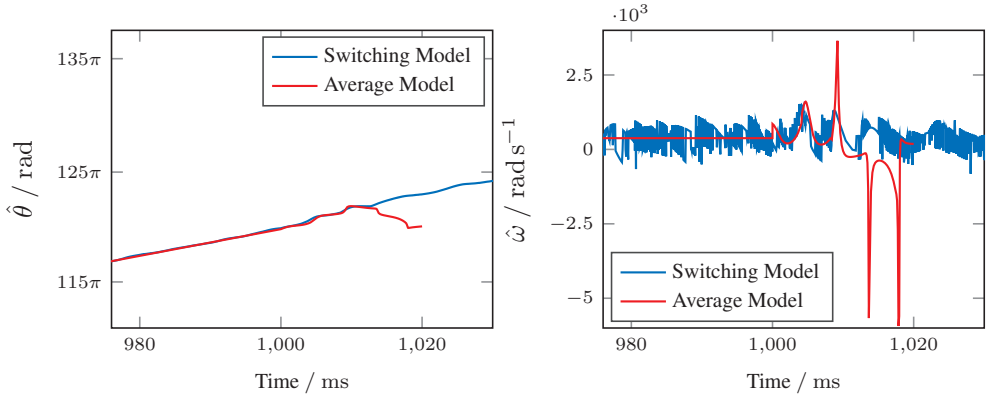

(a) Estimated phase angle **(b)** Estimated frequency

Figure 4.12: Effect of phase shift on PLL output with weak grid connection

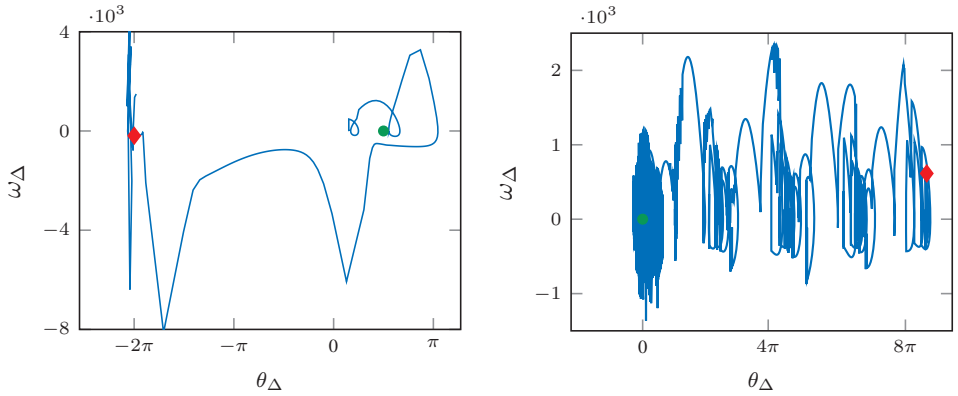

(a) Average model **(b)** Switching model

Figure 4.13: Effect of phase shift on PLL output with weak grid connection

4.2.3 Large Power Step

As demonstrated in [6], marginally stable or unstable behaviour in the VSC power output can be observed after applying a large change in the power reference when the converter is connected to a weak grid. For the simulation, grid line resistance was set to 0.05 Ω and grid line inductance to 8 mH). In this scenario the average model did not yield any significant information before diverging and is not included in the results. Fig. 4.14 shows the active power output of the converter. An initial step in power reference of 1400 W was applied. At $t \approx 230\mathrm{ms}$ there is a large drop in output power. This happens two more times before the converter loses all track of an output resembling the commanded reference.

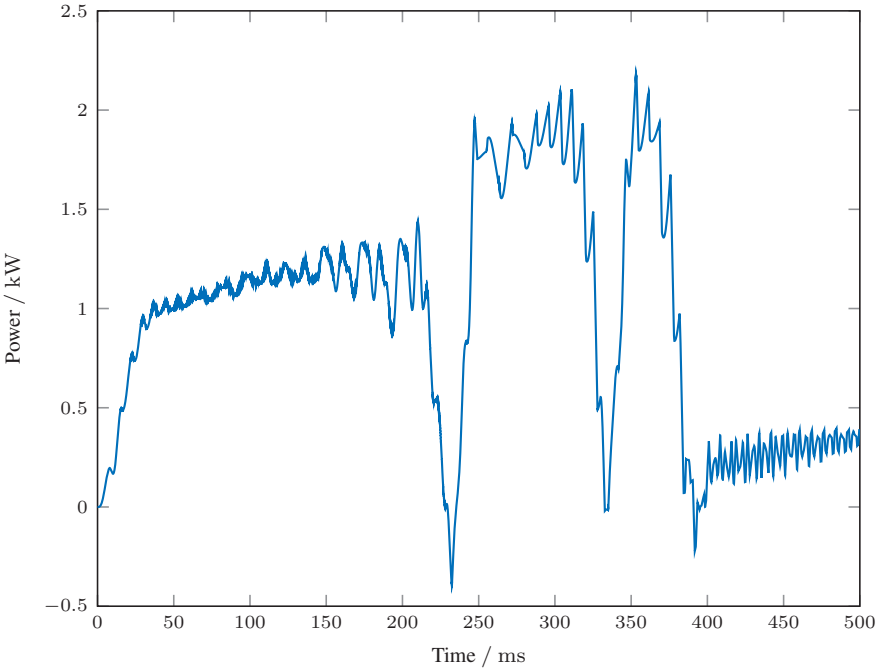

Figure 4.14: Effect of large power reference step at $t = 0$ on active power output with weak grid connection

Fig. 4.15a displays the estimated phase angle for the duration of the simulation. At $t \approx 230\mathrm{ms}$ the phase angle experiences exactly one cycle slip (circled in red). This happens again at $t \approx 330\mathrm{ms}$. A close-up of these events are shown in fig. 4.15b. Lastly, at $t \approx 390\mathrm{ms}$ the correct phase angle is lost for the remainder of the simulation.

Fig. 4.16 exhibits the estimated frequency. At $t \approx 230\mathrm{ms}$ and $t \approx 330\mathrm{ms}$ two large tops are seen (circled in red). From the phase plot, fig. 4.17, it is evident that they stem from the trajectory the PLL is following during the two cycle slips.

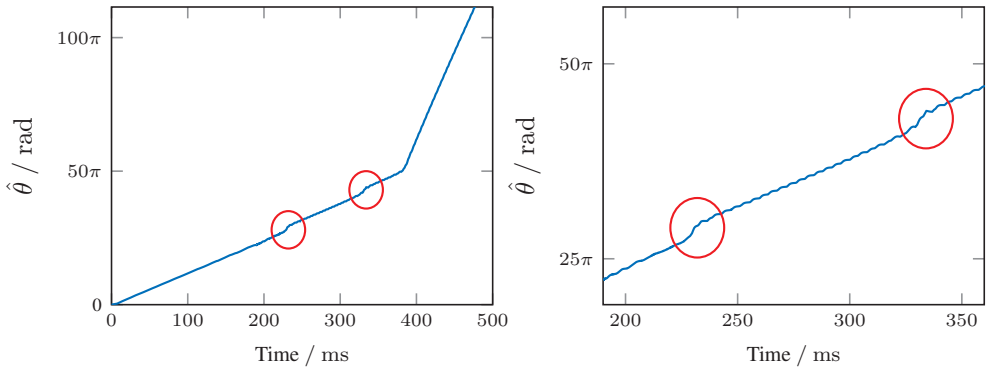

(a) Estimated phase angle **(b)** Close-up of cycle slips

Figure 4.15: Effect of large power reference step at $t = 0$ on $\hat{\theta}$ with weak grid connection

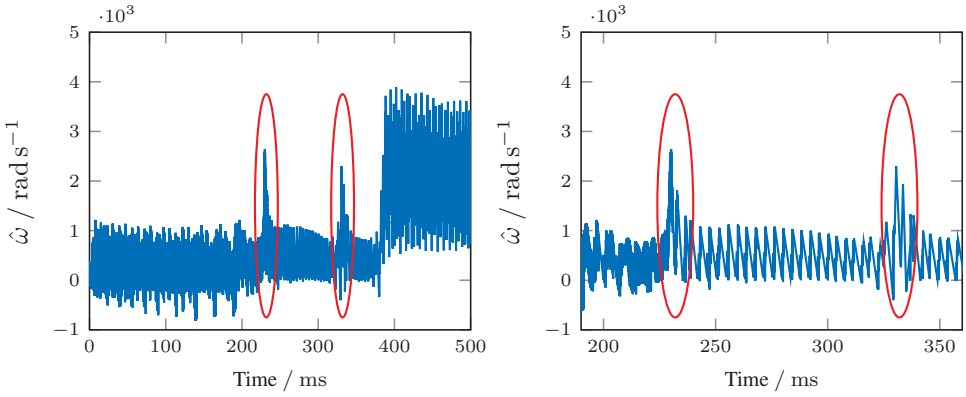

(a) Estimated phase frequency **(b)** Close-up of cycle slips

Figure 4.16: Effect of large power reference step at $t = 0$ on $\hat{\omega}$ with weak grid connection

From fig. 4.17 it is clear that the PLL is leaping from one equilibrium to another. The characteristic valley as the trajectory approaches the unstable saddle points at $\theta_\Delta = \pi,\ 3\pi$ is present, however slightly phase shifted. As with the previous phase plots, the green dot displays the initial phase difference. The red dots show the equilibrium points where the PLL reacquires lock. The data has been low-pass filtered to remove pollution from the switching devices and display the effect more clearly.

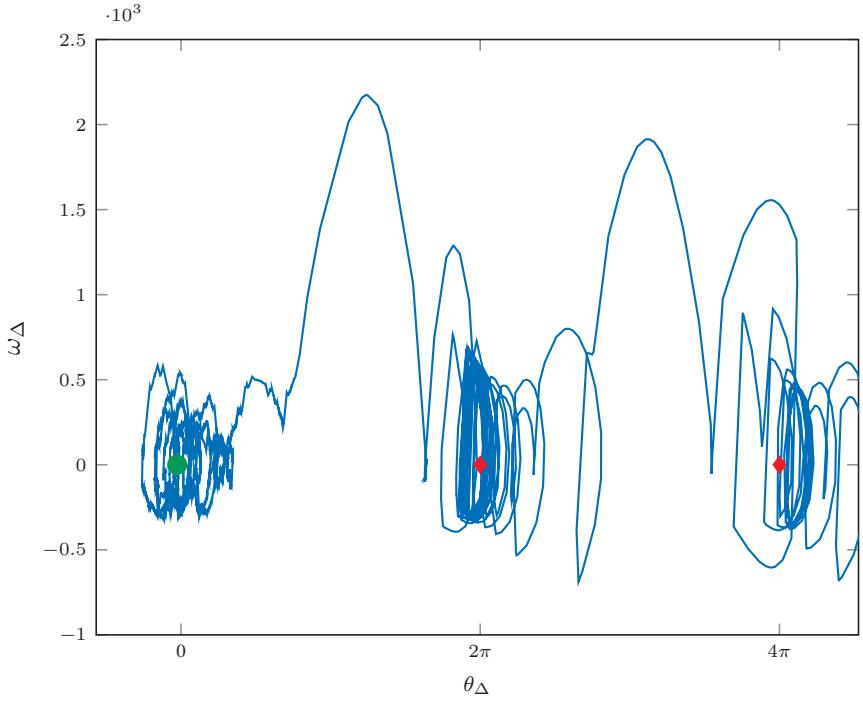

Figure 4.17: Phase-plot of phase and frequency error after a large step in power reference was applied

5 | Discussion

The main question this thesis aims to answer, is whether unstable operation of VSCs used in power systems can be attributed to non-linear behaviour in the SRF-PLL for single-phase systems. Even though the SRF-PLL is proven globally stable with ideal orthogonal signals (section 3.3.2), and is seemingly globally stable with a small difference in true and assumed grid frequency (section 3.5.3), cycle slips lead to undesirable output during the acquisition and/or re-acquisition process. The figures in section 4.2.1 show that cycle slips lead to a transient period of oscillatory behaviour in all components of the VSC, which can be classified as temporarily unstable operation.

5.1 Phase Shift and Cycle Slips

When the converter is connected to a weak grid, what is believed to be cycle slips are observed when an abrupt shift of phase is applied to the grid voltage source V_g (fig. 2.1). Specially fig. 4.13a shows the phase and frequency errors, $\theta_\Delta,\ \omega_\Delta$, following a trajectory towards the unstable saddle point at $(\theta_\Delta,\ \omega_\Delta) = (-\pi, 0)$, before reverting back to a high frequency error. The trajectory is very similar to trajectories shown in figs. 3.3, 3.5 and 3.8, but differs as it crosses from the upper-half plane to the lower at the beginning.

From a mathematical point of view it makes sense that a phase shift could provoke cycle slips. As the derivate of a step function is the impulse function (with infinite magnitude), and the frequency is the derivate of the phase angle, a shift in phase should lead to an infinite impulse in frequency. However, the lock-in range of the PLL is defined for a non-vanishing difference in frequency. This might be the reason why cycle slips are observed only when the converter is connected to a weak grid. The added dynamic effects of the grid possibly enables the frequency disturbance to linger long enough for the PLL to be pushed outside its lock-in range.

In section 4.2.2 the average model does seem to reacquire the correct phase prediction while the more correct switching device model does not. As seen in all simulations, the switching device model does pollute the frequency estimate from the PLL heavily. In addition, the true frequency at PCC is unknown (this is why we use the PLL). It is possible that the noise leads to a high-frequency signal being injected into the grid, and that the PLL lock in to this wrong phase and frequency instead. It is also possible that the PLL is close to regaining stability, as multiple orbits are observed at 2π-periodic intervals in the phase plot fig. 4.13, but the already highly oscillatory behaviour in other parts of the system makes the PLL unable to fully reacquire stability.

5.2 Power Step and Cycle Slips

As demonstrated in section 4.2.3, it is clear that cycle slips occur when the converter is subjected to a large step in commanded power and connected to a weak grid. Especially fig. 4.15 shows strong resemblance to fig. 4.8 where cycle slipping is intentionally provoked. In contrast to the case where a phase shift is applied to the grid source, the step in power has no such obvious source of large frequency disturbance. However, since the difference between the frequency estimate from the PLL and the true grid frequency does not cross the lock-in range, the actual frequency at the point of measurement (PCC) has to be significantly different than the grid frequency, at least for a transient period

The articles [6, 25] trace converter instability back to the PLL, but it can be argued, based on results in section 4.2.3, that the conditions created by the rest of the system enables the PLL to experience cycle slips and provide an incorrect phase angle estimate. Oscillations in the system are significant even before the PLL loses the correct phase angle prediction.

5.3 Lock-In Range

When the phase shift is applied, the PLL cross the lock-in range of approximately 2500 $\mathrm{rad\,s^{-1}}$ before cycle slips occur (fig. 4.12b at $t \approx 1010\mathrm{ms}$). It is believed that while the behaviour is not exactly identical to what is seen in figs. 3.3 and 3.8, the lock-in range is still predictive of when the cycle slip(s) will occur. In fig. 4.12b the average model exhibits two large peaks before the phase angle is lost during the third peak. Why the peaks are increasing in magnitude before slipping occurs is not known. It is also important to note that the lock-in range depends on the true value of ω at PCC, and that this value is not known.

In the case of a large power step, the lock-in range is not crossed by the PLL frequency estimate before cycle slips occur (fig. 4.16, $\hat{\omega}$ is seen oscillating between approximately $\pm 1000\mathrm{rad\,s^{-1}}$). As mentioned in section 5.2 the source of a large frequency disturbance must be in the true ω at PCC. If this parameter is known, it is easy to verify that the difference between estimated and true frequency is larger that the lock-in range, and that cycle slips will occur.

5.4 PLL Parameters

In [6, 25] it is suggested to reduce the PLL gains when instability occurs after large steps in commanded power. This is proved with simulations and presented as a solution to the problem. As the PLL responds slowly to a frequency disturbance, errors in the frequency estimate will propagate gradually through the current controller and be fed back to the PLL. This might be enough to keep the system stable while the disturbance is damped. What might be overlooked is that the lock-in range will be reduced accordingly. If the

gains are reduced significantly, the system might be prone to cycle slips and instability at very low frequency disturbances, even though the large steps in power work fine. The self-created disturbance originating in the feedback loop from the converter terminal to the control systems might be damped with lowered PLL parameters, but an external perturbation originating in the grid connection might force the PLL over the lock-in range and cycle slips will occur.

6 | Conclusion

The SRF-PLL for single-phase systems is shown to be globally stable under ideal conditions, and probably globally stable when the time delay, used to construct the orthogonal component, is slightly wrong. A non-linear effect called cycle slip can still contribute to large errors in both phase and frequency before the system reaches equilibrium as $t \to \infty$.

Based on the results obtained from simulation, it is demonstrated that non-linear behaviour in the SRF-PLL can be present and lead to unstable operation of the entire voltage source converter. Fig. 4.13 shows what is believed to be cycle slipping when a phase jump is applied to the grid voltage source. Figs. 4.15 and 4.17 show cycle slipping when a step in reference is applied to the active power controller. Fig. 4.15b clearly displays the same effect as fig. 4.8, where cycle slipping is intentionally provoked.

As more variable renewable energy, HVDC-interconnections and associated voltage source converters are connected to the main utility grid, it is important to understand the limits of stable operation for the converter. This thesis should deliver a step toward fully understanding the mechanisms leading to unstable operation of the VSC and it should be clear that analysis of the PLL applied to power converter systems have to be carried out with the non-linear domain in mind.

6.1 Further Work

This thesis might serve as a starting point for non-linear analysis of the phase-locked loop applied to power converter systems. As a consequence, further work can go in multiple directions:

- Establishing the relationship between the weak grid parameters, the step in power reference and the lock-in range. This would enable us to construct a guaranteed range of safe operation based on these parameters and the PLL gains.
- Examining whether other, more complicated PLL systems (such as the SOGI-PLL [24]) are prone to the same non-linear effects.
- Verifying that the same effects are present in three-phase systems. This is believed to be true because the DQ transform translates both three-phase and single-phase systems to the same representation, however variations might be present when errors occur.

A | Equilibrium Point

$$K_1 = 8\omega\cos(2\omega t)T_i\cos\left(\frac{\omega\pi}{\omega_0}\right) + 8\sin(2\omega t)\sin\left(\frac{\omega\pi}{\omega_0}\right)T_i\omega + 16\cos\left(\frac{\omega\pi}{2\omega_0}\right)T_i\omega\sin(2\omega t)$$
$$+ 8\omega\cos(2\omega t)T_i - 2\sin\left(\frac{\omega\pi}{\omega_0}\right)\cos(2\omega t) - 4\cos\left(\frac{\omega\pi}{2\omega_0}\right)\cos(2\omega t) + 2\sin(2\omega t)\cos\left(\frac{\omega\pi}{\omega_0}\right)$$

$$\begin{aligned}
K_2 = {} & \Big((64T_i^2\omega^2 - 4)\cos(4\omega t) + 64T_i^2\omega^2 + 32T_i\omega\sin(4\omega t) + 12\Big)\sin\left(\frac{\omega\pi}{2\omega_0}\right) \\
& + \Big((64T_i^2\omega^2 - 4)\cos(4\omega t) + 64T_i^2\omega^2 + 32T_i\omega\sin(4\omega t) + 12\Big)\sin\left(\frac{3\omega\pi}{2\omega_0}\right) \\
& + \Big(-192T_i^2\omega^2\sin(4\omega t) + 96\omega T_i\cos(4\omega t) + 12\sin(4\omega t)\Big)\cos\left(\frac{\omega\pi}{2\omega_0}\right) \\
& + \Big(-64T_i^2\omega^2\sin(4\omega t) + 32\omega T_i\cos(4\omega t) + 4\sin(4\omega t)\Big)\cos\left(\frac{3\omega\pi}{2\omega_0}\right) \\
& + \Big(32\cos(4\omega t)T_i^2\omega^2 + 16T_i\omega\sin(4\omega t) - 2\cos(4\omega t)\Big)\cos\left(\frac{2\omega\pi}{\omega_0}\right) \\
& + \Big(32T_i^2\omega^2\sin(4\omega t) - 16\omega T_i\cos(4\omega t) - 2\sin(4\omega t)\Big)\sin\left(\frac{2\omega\pi}{\omega_0}\right) \\
& + \Big(64T_i^2\omega^2\sin(4\omega t) - 32\omega T_i\cos(4\omega t) - 4\sin(4\omega t)\Big)\sin\left(\frac{\omega\pi}{\omega_0}\right) \\
& - 32\cos(4\omega t)T_i^2\omega^2 - 128\cos\left(\frac{\omega\pi}{\omega_0}\right)T_i^2\omega^2 \\
& - 128T_i^2\omega^2 - 16T_i\omega\sin(4\omega t) + 2\cos(4\omega t) + 8\cos\left(\frac{\omega\pi}{\omega_0}\right) + 8
\end{aligned}$$

$$Y = \Big(K_1 - \sqrt{K_2} + 2\sin(2\omega t)\Big)\left(\sin\left(\frac{\omega\pi}{2\omega_0}\right) - 1\right)\left(\cos\left(\frac{\omega\pi}{2\omega_0}\right)\right)^{-2} \tag{A.1}$$

$$K_3 = -8\sin(2\omega t)\sin\left(\frac{\omega\pi}{\omega_0}\right)T_i\omega - 32\sin\left(\frac{\omega\pi}{2\omega_0}\right)\cos(2\omega t)T_i\omega + 16\cos\left(\frac{\omega\pi}{2\omega_0}\right)T_i\omega\sin(2\omega t)$$
$$- 8\omega\cos(2\omega t)T_i\cos\left(\frac{\omega\pi}{\omega_0}\right) + 24\omega\cos(2\omega t)T_i + 2\sin\left(\frac{\omega\pi}{\omega_0}\right)\cos(2\omega t)$$
$$- 8\sin(2\omega t)\sin\left(\frac{\omega\pi}{2\omega_0}\right) - 4\cos\left(\frac{\omega\pi}{2\omega_0}\right)\cos(2\omega t) - 2\sin(2\omega t)\cos\left(\frac{\omega\pi}{\omega_0}\right)$$

$$K_4 = \Big((64T_i^2\omega^2 - 4)\cos(4\omega t) + 64T_i^2\omega^2 + 32T_i\omega\sin(4\omega t) + 12\Big)\sin\left(\frac{\omega\pi}{2\omega_0}\right)$$
$$+ \Big((64T_i^2\omega^2 - 4)\cos(4\omega t) + 64T_i^2\omega^2 + 32T_i\omega\sin(4\omega t) + 12\Big)\sin\left(\frac{3\omega\pi}{2\omega_0}\right)$$
$$+ \Big(-192T_i^2\omega^2\sin(4\omega t) + 96\omega T_i\cos(4\omega t) + 12\sin(4\omega t)\Big)\cos\left(\frac{\omega\pi}{2\omega_0}\right)$$
$$+ \Big(-64T_i^2\omega^2\sin(4\omega t) + 32\omega T_i\cos(4\omega t) + 4\sin(4\omega t)\Big)\cos\left(\frac{3\omega\pi}{2\omega_0}\right)$$
$$+ \Big(32\cos(4\omega t)T_i^2\omega^2 + 16T_i\omega\sin(4\omega t) - 2\cos(4\omega t)\Big)\cos\left(\frac{2\omega\pi}{\omega_0}\right)$$
$$+ \Big(32T_i^2\omega^2\sin(4\omega t) - 16\omega T_i\cos(4\omega t) - 2\sin(4\omega t)\Big)\sin\left(\frac{2\omega\pi}{\omega_0}\right)$$
$$+ \Big(64T_i^2\omega^2\sin(4\omega t) - 32\omega T_i\cos(4\omega t) - 4\sin(4\omega t)\Big)\sin\left(\frac{\omega\pi}{\omega_0}\right)$$
$$- 32\cos(4\omega t)T_i^2\omega^2 - 128\cos\left(\frac{\omega\pi}{\omega_0}\right)T_i^2\omega^2 - 128T_i^2\omega^2$$
$$- 16T_i\omega\sin(4\omega t) + 2\cos(4\omega t) + 8\cos\left(\frac{\omega\pi}{\omega_0}\right) + 8$$

$$X = \Big(K_3 + \sqrt{K_4} + 6\sin(2\omega t)\Big)\left(\cos\left(\frac{\omega\pi}{2\omega_0}\right)\right)^{-1} \tag{A.2}$$

$$x_{1_{eq}} = \arctan(Y, X) \tag{A.3}$$

B | Additional Simulations

B.1 Provoked Cycle Slips with Grid Connection

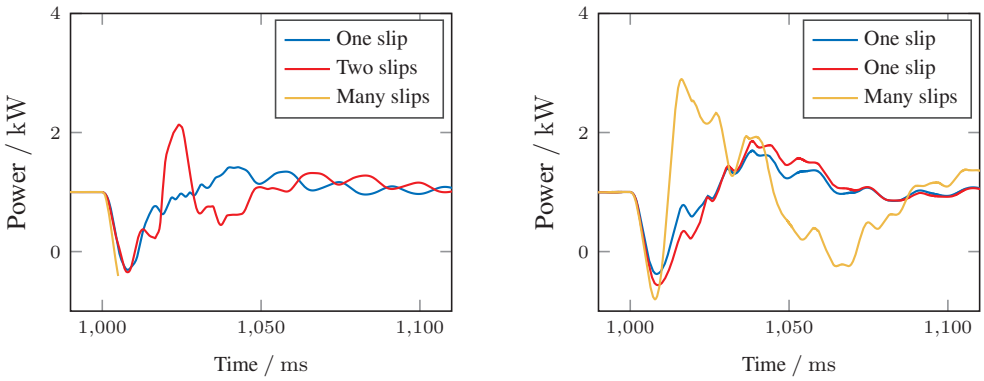

(a) Average model **(b)** Switching device model

Figure B.1: Comparison of active power output for the two models exposed to cycle slips. Note that the last average model simulations was stopped early

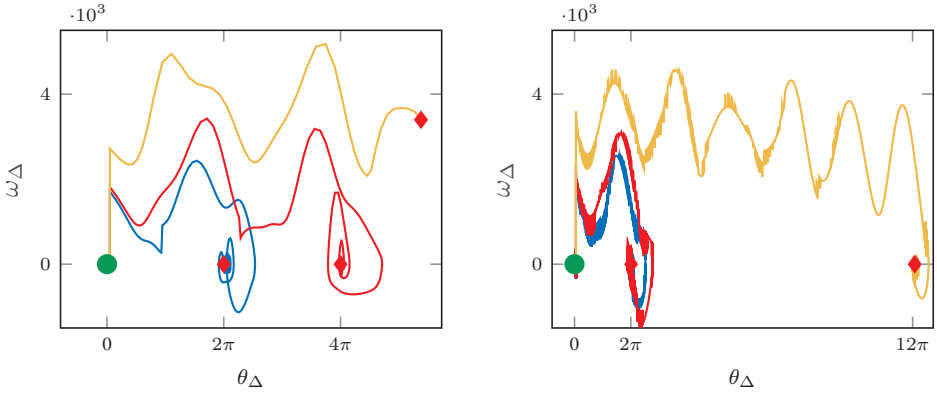

(a) Average model **(b)** Switching device model

Figure B.2: Phase plots for the two models exposed to cycle slips. Note that the last average model simulations was stopped early

C | Simulink Models

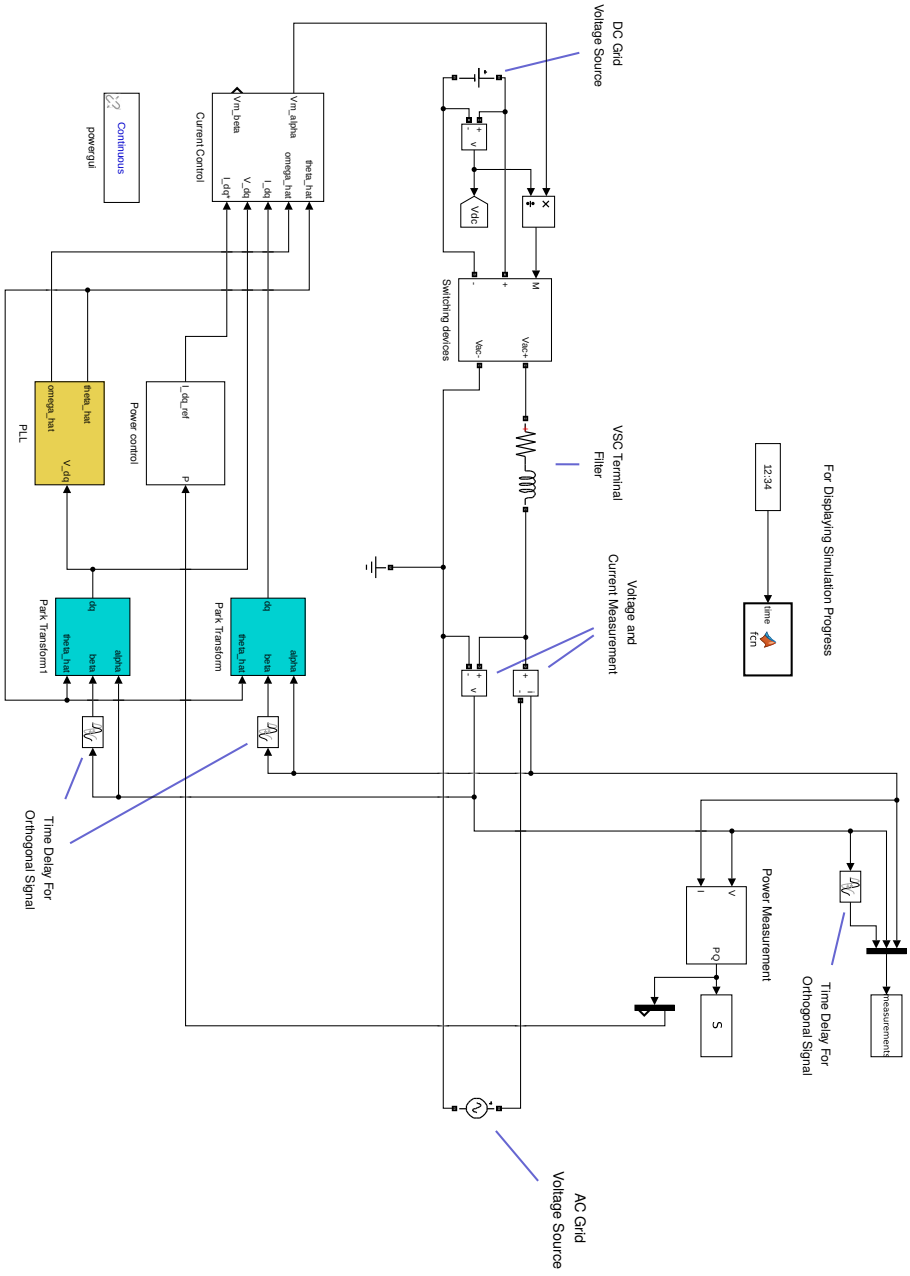

Figure C.1: Simulink model without grid transmission line

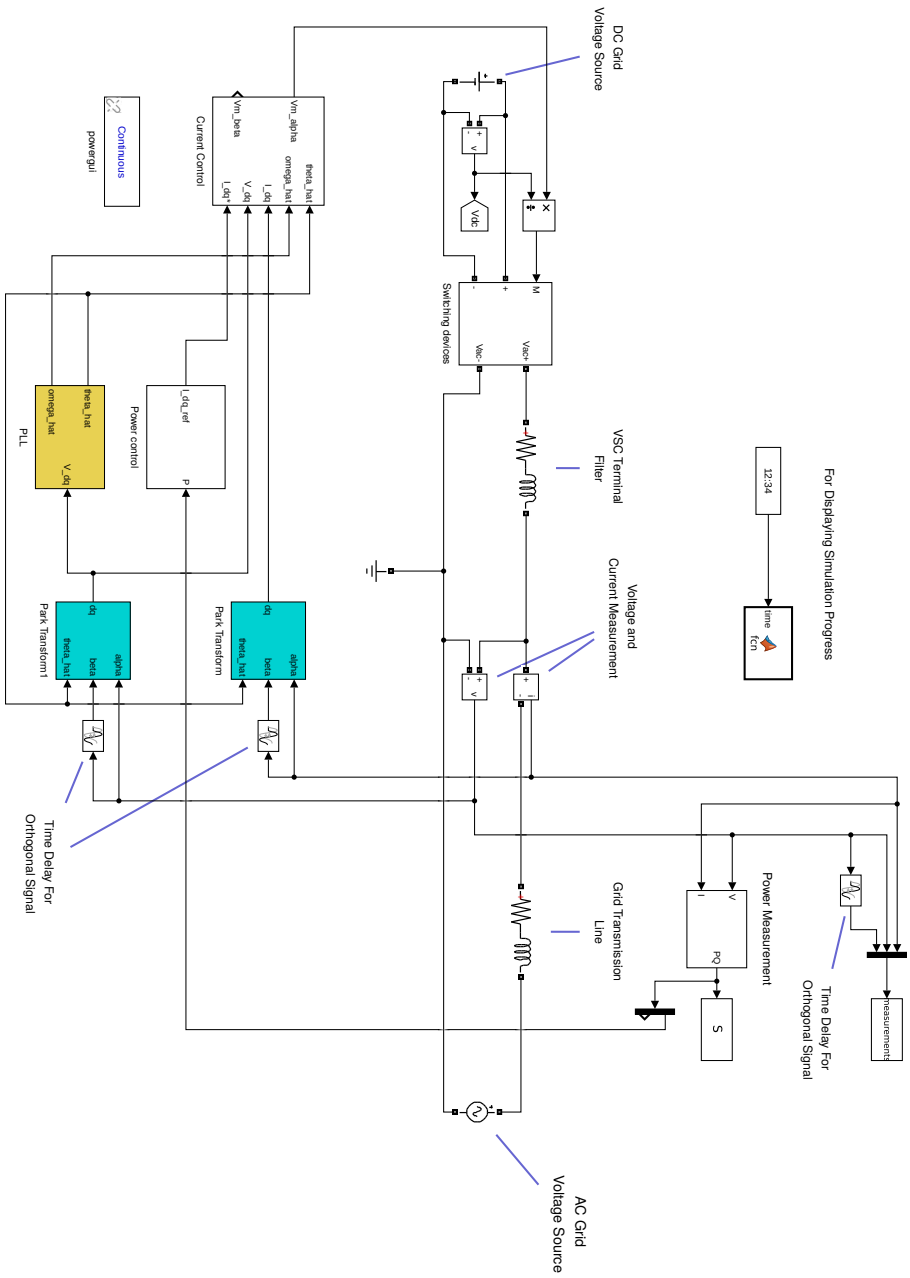

Figure C.2: Simulink model with grid transmission line

The full *Matlab* scripts and *Simulink* models can be found either attached as an electronic appendix or from `https://github.com/sigurdjs/Nonlinear_PLL`.

Bibliography

[1] Geoffrey Carr. *Sunny Uplands*. Ed. by The Economist. https://www.economist.com/news/21566414-alternative-energy-will-no-longer-be-alternative-sunny-uplands. 2012.

[2] Fraunhofer Institute for Solar Energy Systems. *30.2 Percent Efficiency New Record for Silicon-based Multi-junction Solar Cell*. https://www.ise.fraunhofer.de/en/press-media/press-releases/2016/30-2-percent-efficiency-new-record-for-silicon-based-multi-junction-solar-cell.html. 2016.

[3] Jess Shankleman and Brian Parkin. *Wind Power Blows Through Nuclear, Coal as Costs Drop at Sea*. Ed. by Bloomberg. https://www.bloomberg.com/news/articles/2017-03-09/wind-power-blows-through-nuclear-coal-as-costs-plunge-at-sea. 2017.

[4] Magnus Callavik. *HVDC interconnectors enable a stronger smarter and greener grid*. https://www.abb-conversations.com/2017/11/hvdc-interconnectors-enable-a-stronger-smarter-and-greener-grid/. 2017.

[5] Jos Arrillaga et al. *Self-Commutating Converters for High Power Applications*. 2009.

[6] Jenny Z. Zhou and Aniruddha M. Gole. "VSC transmission limitations imposed by AC system strength and AC impedance characteristics". In: *IEEE* (2013). https://ieeexplore.ieee.org/document/6521285/.

[7] Anders Rantzer. "Almost global stability of phase-locked loops". In: *IEEE* (2001). http://www.control.lth.se/documents/2001/Rantzer01c.pdf.

[8] Leonov G.A. et al. "Hold-in, pull-in, and lock-in ranges of PLL circuits: rigorous mathematical definitions and limitations of classical theory". In: *IEEE* (2015). https://ieeexplore.ieee.org/document/7277189/.

[9] Konstantin D. Alexandrov et al. "Pull-in range of the PLL-based circuits with proportionally-integrating filter". In: *IFAC-PapersOnLine* (2015). https://www.sciencedirect.com/science/article/pii/S2405896315013555.

[10] Konstantin D. Aleksandrov et al. "Computation of the lock-in ranges of phase-locked loops with PI filter". In: *IFAC-PapersOnLine* 49.14 (2016). http://www.sciencedirect.com/science/article/pii/S2405896316312599, pp. 36–41.

[11] Mohammad Amin. “Small-signal Stability Characterization of Interaction Phenomena between HVDC System and Wind Farms”. https://brage.bibsys.no/xmlui/handle/11250/2451148. PhD thesis. NTNU, 2017.

[12] Chengyong Zhao and Chunyi Guo. “Complete-Independent Control Strategy of Active and Reactive Power for VSC Based HVDC System”. In: *IEEE* (2009). http://ieeexplore.ieee.org/document/5275743/.

[13] Jaime Peralta et al. “Dynamic Performance of Average-Value Models for Multi-terminal VSC-HVDC Systems”. In: *IEEE* (2012). http://ieeexplore.ieee.org/document/6345610.

[14] Saeed Golestan, Mohammad Monfared, and Francisco D. Freijedo. “Performance Improvement of a Prefiltered Synchronous-Reference-Frame PLL by Using a PID-Type Loop Filter”. In: *IEEE* (2014). http://ieeexplore.ieee.org/document/6603275/.

[15] W. Wang et al. “Analysis of Active Power Control for VSC”. In: *IEEE Transactions on Power Delivery* (2014). https://ieeexplore.ieee.org/document/6824844/.

[16] T. Midtsund, J. A. Suul, and T. Undeland. “Evaluation of current controller performance and stability for voltage source converters connected to a weak grid”. In: *The 2nd International Symposium on Power Electronics for Distributed Generation Systems*. https://ieeexplore.ieee.org/document/5545794/. 2010.

[17] Hassan K. Khalil. *Nonlinear Systems*. 2002.

[18] Floyd Martin Gardner. *Phaselock techniques*. 1966.

[19] F. Gonzalez-Espin, E. Figueres, and G. Garcera. “An Adaptive Synchronous-Reference-Frame Phase-Locked Loop for Power Quality Improvement in a Polluted Utility Grid”. In: *IEEE Transactions on Industrial Electronics* (2012). https://ieeexplore.ieee.org/document/6032093/.

[20] D. Jovcic. “Phase locked loop system for FACTS”. In: *IEEE Transactions on Power Systems* (2003). https://ieeexplore.ieee.org/abstract/document/1216154/.

[21] Se-Kyo Chung. “A Phase Tracking System for Three Phase Utility Interface Inverters”. In: *IEEE* (2000). http://ieeexplore.ieee.org/document/844502/.

[22] Philip Hartman. *Ordinary Differential Equations*. 1964.

[23] Konstantin Aleksandrov. “Phase-locked loops with active PI filter: the lock-in range computation”. https://jyx.jyu.fi/dspace/handle/123456789/50153. PhD thesis. University of Jyväskylä, 2016.

[24] Mihai Ciobotaru, Remus Teodorescu, and Frede Blaabjerg. “A New Single-Phase PLL Structure Based on Second Order Generalized Integrator”. In: *IEEE* (2006). http://ieeexplore.ieee.org/document/1711988/.

[25] J. Z. Zhou et al. “Impact of Short-Circuit Ratio and Phase-Locked-Loop Parameters on the Small-Signal Behavior of a VSC-HVDC Converter”. In: *IEEE Transactions on Power Delivery* (2014). https://ieeexplore.ieee.org/document/7741107/.